

1 Highlights

2 1. Stepwise including topography and vegetation improved runoff and
3 snow simulations.

4 2. The ratio of snowmelt runoff to streamflow was 23.6% and 15.9% in
5 two Mongolian basins.

6 3. High elevations showed slower snowmelt release; low elevations
7 generate rapid, rainfall-driven runoff.

8

9

10

11

12

13

14

15

16

17

18

19

20

21

22

23 **Revealing the Influence of Topography and Vegetation on**
24 **Hydrological Processes Using a Stepwise Modelling Approach in Cold**
25 **Alpine Basins of the Mongolian Plateau**

26 Leilei Yong ¹, Yahui Wang ¹, Batsuren Dorjsuren ², Zheng Duan ³, Hongkai
27 Gao ^{1*}

28 ¹ Key Laboratory of Geographic Information Science (Ministry of
29 Education of China), School of Geographical Sciences, East China Normal
30 University, Shanghai, China

31 ² Department of Environment and Forest Engineering, National University
32 of Mongolia, Ulaanbaatar 210646, Mongolia

33 ³ Department of Physical Geography and Ecosystem Science, Lund
34 University, Sölvegatan 12, SE-223 62, Lund, Sweden

35

36 * Correspondence: Hongkai Gao, hkgao@geo.ecnu.edu.cn

37

38 **Abstract:** Topography and vegetation are critical factors influencing catchment
39 hydrology; however, their individual contributions are often underestimated in
40 hydrological models. This limitation is particularly evident in cold, mountainous
41 regions such as the Mongolian Plateau, where observational data are sparse. To address
42 this, we employed a stepwise, top-down modelling strategy based on a flexible
43 modelling framework to systematically assess the influence of topography and
44 vegetation on hydrological processes in the Bogd Uliastai and Zavkhan Guulin river
45 basins. Beginning with a lumped model (FLEX^L), we successively integrated snow
46 processes (FLEX^L-S), topographic distribution (FLEX^D), and finally, a landscape-based
47 parameterization accounting for vegetation heterogeneity (FLEX^T). Both FLEX^D and

48 FLEX^T outperformed the lumped models in simulating runoff and snow water
49 equivalent (SWE). Interestingly, FLEX^T showed similar performance to FLEX^D—
50 likely due to limited vegetation heterogeneity—it offers more physically realistic
51 parameterization by explicitly representing landscape units, suggesting its potential in
52 more complex basins. The ratio of snowmelt runoff to streamflow was quantified as
53 23.6%±0.7% and 15.9%±1.3% in the Bogd Uliastai and Zavkhan Guulin river basins,
54 respectively, with peaks in spring and a clear increase with elevation. At high elevations,
55 runoff is primarily snowmelt-driven, resulting in delayed and gradual runoff, whereas
56 lower elevations dominated by rainfall generate rapid runoff. Controlled by distinct
57 dominant hydrological mechanisms, different landscape units contribute unequally to
58 streamflow. This study underscores the pivotal roles of topography and vegetation in
59 runoff generation and demonstrates the effectiveness of a stepwise modelling
60 framework for improving hydrological understanding in cryospheric and data-scarce
61 regions.

62 **Keywords:** Mongolian Plateau, FLEX model, stepwise modelling framework,
63 snowmelt, topography, vegetation

64

65 **1. Introduction**

66 Understanding and accurately simulating hydrological processes are fundamental for
67 elucidating basin hydrological patterns and supporting water resource management and
68 ecological protection under global environmental change (Gomes et al., 2023; Oki and
69 Kanae, 2006). Topography and vegetation play essential roles as drivers of hydrological
70 processes, influencing precipitation, interception (Dwarakish and Ganasri, 2015),
71 snowmelt (Hammond et al., 2019), evaporation (Jiao et al., 2017), and runoff generation
72 (Qin et al., 2025). Their combined influence underpins landscape organization, forms
73 the basis for Hydrological Response Units (HRUs), and shapes spatial heterogeneity
74 and dominant hydrological mechanisms (Savenije, 2010; Sivapalan, 2009). Limited
75 observational data in cold-arid regions often results in oversimplified hydrological

76 models, emphasizing the need to represent landscape controls more explicitly (Ragetti
77 et al., 2014; Tarasova et al., 2016).

78
79 Topography governs water redistribution across landscapes by shaping soil moisture
80 patterns, modulating precipitation and evaporation, and controlling runoff pathways
81 (Wicki et al., 2023). In mountainous basins, strong relief introduces substantial
82 challenges for hydrological modelling and increase predictive uncertainty (Seibert and
83 McDonnell, 2002). Steeper slopes typically lead to more rapid runoff, while gentler
84 slopes promote greater infiltration and moisture retention, thereby affecting the
85 spatiotemporal distribution of water resources (Ye et al., 2023). In addition, topographic
86 features such as slope, aspect, and elevation control snow accumulation and melt,
87 resulting in highly heterogeneous hydrological responses across basins (Broxton et al.,
88 2020).

89
90 Vegetation also regulates hydrological processes by intercepting snow and rainfall,
91 facilitating water infiltration and storage in the root zone, and absorbing and transpiring
92 water through its roots. Canopies reduce effective precipitation reaching the ground and
93 can mitigate surface runoff (Cheng et al., 2020), while root systems shape soil moisture
94 dynamics and water redistribution (Luo et al., 2022; Volpe et al., 2013). Consequently,
95 different vegetation types (e.g., forests, grassland, and abandoned farmland) often
96 exhibit distinct hydrological behaviors (Chen et al., 2023). In cold mountainous regions,
97 vegetation further alters snow processes through shading and moderating wind
98 redistribution, thereby influencing the meltwater timing and magnitude (Sun et al.,
99 2022). Over long timescales, snow-vegetation interactions can modulate runoff
100 sensitivity to precipitation, evapotranspiration, and vegetation dynamics, especially in
101 regions such as Central Asia (Feng et al., 2025) and the Tibetan Plateau (Ni et al., 2025).

102
103 Despite the recognized importance of topography and vegetation, their influences
104 remain insufficiently represented in many hydrological modelling frameworks

105 (Stephens et al., 2021). This gap is especially critical in cryospheric regions, where
106 snow accumulation and melt dominate runoff generation and are strongly shaped by
107 terrain and vegetation controls (Dharmadasa et al., 2023; Immerzeel et al., 2010; Zhong
108 et al., 2021). Quantifying and integrating these controls into hydrological models is
109 therefore essential for advancing cold-region hydrology and improving model realism.

110

111 Existing hydrological models often struggle to adequately capture the complexities
112 introduced by topography and vegetation heterogeneity. Early lumped models, relying
113 on basin-averaged inputs, oversimplify spatial heterogeneity within catchments (Beven,
114 2012). Distributed hydrological models allow spatially explicit simulations but are
115 highly dependent on the availability and quality of input data (Fenicia et al., 2016),
116 which remains a significant limitation in cold, high-mountain regions. Remote sensing
117 has become an invaluable tool for providing spatially continuous data on topography
118 (e.g., Digital Elevation Models, DEMs), vegetation (e.g., Normalized Difference
119 Vegetation Index (NDVI) and Enhanced Vegetation Index (EVI)) (Xiong et al., 2023),
120 and snow dynamics (e.g., SWE) (Duethmann et al., 2014), enabling a more realistic
121 representation of landscape-dependent controls in hydrological models (Gao et al.,
122 2014).

123

124 In the absence of direct measurements of individual hydrological processes, the top-
125 down modelling approach offers a powerful and practical means of exploring the
126 internal dynamics of basin behavior (Fenicia et al., 2008b). Originally proposed by
127 Klemeš (Klemeš, 1983) and later reformulated by Sivapalan et al. (Sivapalan et al.,
128 2003), the top-down approach is rooted in a deductive philosophy that infers the
129 underlying ‘causes’ from the overall observed ‘effect’ of a system. In hydrological
130 modelling, this method begins with a simple structure that is progressively refined to
131 address limitations in reproducing observed catchment behavior (Fenicia et al., 2008a).

132

133 The Bogd Uliastai and Zavkhan Guulin river basins, in the headwaters of the Zavkhan

134 River on the western Mongolian Plateau, exhibit a cold, arid continental climate with
135 sparse vegetation (Baasanmunkh et al., 2019). Strong cryospheric influences control
136 hydrological processes, making these basins key areas for regional ecological security
137 and downstream water-resource resilience. However, monitoring networks are sparse
138 and long-term observational data are limited, leaving runoff generation mechanisms
139 and their interactions with topography, vegetation and the cryosphere poorly understood
140 (Dorjsuren et al., 2024).

141

142 To address these challenges, we employ a top-down modelling framework that begins
143 with a lumped model to assess runoff dynamics and progressively incorporates
144 distributed representations of snowmelt, topography, and vegetation. This framework
145 allows assessment of hydrological responses across different landscape units and
146 addresses three research questions:

- 147 (1) How can runoff be effectively simulated in data-scarce, cold mountainous regions
148 using a top-down modelling approach?
149 (2) How can the contribution of snowmelt runoff to streamflow be quantified using a
150 landscape-based hydrological model?
151 (3) How do topography and vegetation influence runoff generation processes?

152

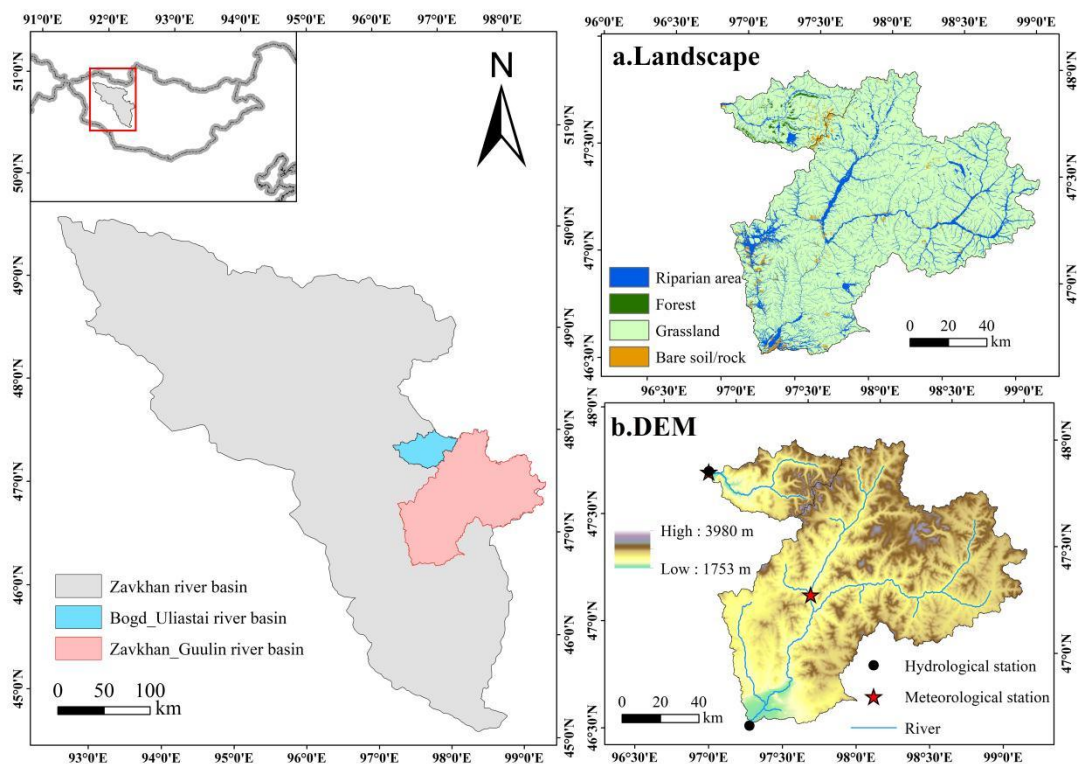
153 The study aligns with the IAHS HELPING Decade (Hydrology Engaging Local People
154 IN one Global world, 2023–2032), which calls for interdisciplinary research in data-
155 scarce and ecologically vulnerable regions. By developing a modelling framework for
156 cold basins with limited observational data and improving understanding of
157 hydrological processes on the Mongolian Plateau, this work provides an important case
158 study contributing to the goals of the HELPING initiative.

159

160 **2. Study site**

161 **2.1 Bogd Uliastai river basin**

162 The Bogd Uliastai river basin (47°30'N-48°10'N, 96°45'E-97°45'E) is located in the
 163 northern part of the Zavkhan river headwaters, along the southern foothills of the central
 164 Khangai Mountains in Mongolia (Fig.1). The basin spans an area of 1610 km² and is
 165 predominantly mountainous, with elevations ranging from 1753 m a.s.l. to 3972 m a.s.l.
 166 The region receives an average annual precipitation of approximately 200 mm, with
 167 more than 80% of rainfall occurring between June and September. The average annual
 168 temperature is -1°C, while winter temperatures frequently fall below -30°C, reflecting
 169 a typical alpine climate. Runoff displays strong seasonal variability, with distinct peaks
 170 during the spring and summer and almost no flow in winter, resulting in extreme
 171 hydrological conditions (Dorjsuren et al., 2024). The vegetation exhibits clear
 172 altitudinal zonation: alpine meadows and tundra, dominated by mosses and lichens,
 173 prevail at higher elevations, whereas needlegrass steppe and low shrublands are
 174 common in mid and low elevation areas (Baasanmunkh et al., 2019).
 175



176
 177 **Fig.1** Location, landscape (a) and topography (b) of the Bogd Uliastai and Zavkhan Guulin river
 178 basins on the Mongolian Plateau.
 179

180 **2.2 Zavkhan Guulin river basin**

181 The Zavkhan Guulin river basin (46°30'N-47°50'N, 96°45'E-97°00'E), located in the
182 central and southern parts of Zavkhan Province, lies within the transitional zone of the
183 southern Khangai Mountains (Fig.1). The basin covers an area of approximately 12258
184 km² and is predominantly composed of low mountains and hills, with elevations
185 ranging from 1785 m a.s.l. to 3980 m a.s.l. The basin's annual average precipitation is
186 about 160 mm, with most precipitation concentrated in summer. The annual average
187 temperature is approximately -3°C, with summer temperatures exceeding 20°C and
188 winter temperatures dropping as low as -50°C, characteristic of a temperate continental
189 climate (Dorjsuren et al., 2023). Vegetation in the region is sparse, primarily dominated
190 by drought-tolerant *Artemisia* species, with scattered distributions of grass and shrubs.
191 At higher elevations, the landscape is characterized by alpine meadows, exposed rock
192 surfaces, and cold desert environments. Soils are nutrient-poor, and the ecological
193 environment is fragile, facing severe challenges such as soil erosion (Baasanmunkh et
194 al., 2019).

195

196 **3. Data**

197 **3.1 Data set**

198 **Hydrometeorological data:** Daily precipitation, runoff, and temperature data for the
199 Bogd Uliastai river basin (2007–2015) and the Zavkhan Guulin river basin (2000–2020)
200 were obtained from the Information and Research Institute of Meteorology, Hydrology,
201 and Environment (IRIMHE) via its official website (<http://irimhe.namem.gov.mn>). For
202 each basin, one meteorological station and one hydrological station served as the
203 primary sources of observational data. The Arctic Snow Water Equivalent (SWE) Grid
204 Dataset (2003–2016) was obtained from National Tibetan Plateau/Third Pole
205 Environment Data Center (<https://cstr.cn/18406.11.Snow.tpd.c.271556>). The SWE
206 product has a daily temporal resolution and a spatial resolution of 10 km, covering
207 latitudes from 45°N to 90°N and longitudes from 180°W to 180°E.

208 **Topographic data:** The Shuttle Radar Topography Mission Digital Elevation Model
209 (SRTM-DEM), with a spatial resolution of 90 m, was acquired from the official website
210 of the CGIAR Consortium for Spatial Information (CGIAR-CSI)
211 (<http://srtm.csi.cgiar.org>).

212 **Land cover data:** The Sentinel-2 10-Meter Land Use/Land Cover was accessed via
213 ESRI's official platform (<https://livingatlas.arcgis.com/landcover/>).

214 **NDVI data:** The normalized difference vegetation index (NDVI) data (2013–2020)
215 were derived from the Landsat 8 Operational Land Imager (OLI) Level-2 surface
216 reflectance products. NDVI was calculated as $(NIR - Red)/(NIR + Red)$ using bands
217 5 (NIR) and 4 (Red). The dataset has a spatial resolution of 30 m and a temporal
218 resolution of 16 days. Landsat data were obtained from the United States Geological
219 Survey (USGS) EarthExplorer platform (<https://earthexplorer.usgs.gov/>).

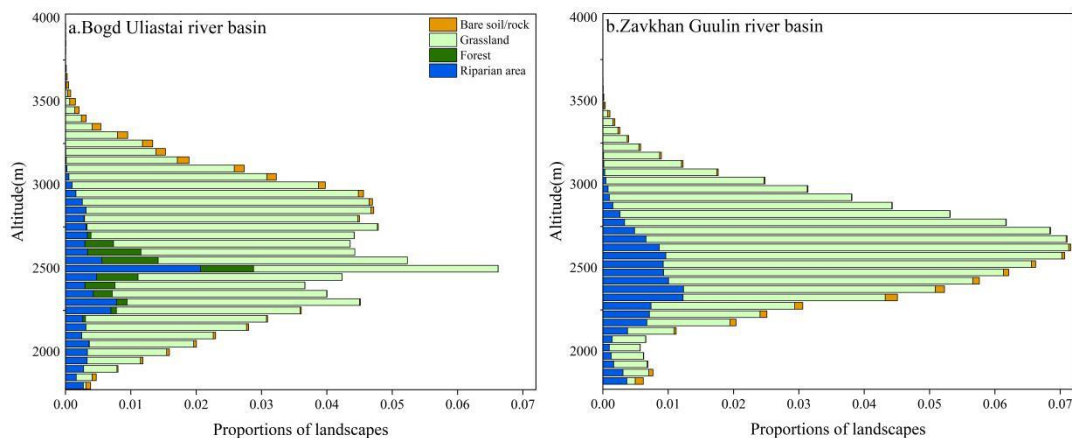
220

221 **3.2 Distribution of forcing data**

222 Mountainous terrain is complex, and meteorological stations are typically located at
223 lower elevations. Directly using point-based measurement in basin-scale simulations
224 without accounting for elevation effects can introduce biases (Klemeš, 1989). In cold
225 mountainous regions, higher elevations typically experience lower temperatures and
226 greater precipitation, often in the form of snow (Lundquist et al., 2010; Stahl et al.,
227 2006). In the study, the FLEX^D and FLEX^T models divide catchment into elevation
228 bands and adjusts temperature and precipitation for each band using a precipitation
229 increase rate and temperature lapse rate (Fig.2). This distributed input approach
230 effectively mitigates simulation bias by better capturing altitudinal variability in
231 meteorological conditions. In this study, due to the remoteness of the region and the
232 sparse distribution of meteorological stations, available ground observations were
233 limited. Satellite and reanalysis products (e.g., ERA5-Land) exhibit notable biases over
234 complex terrain and fail to capture local climatic variability. We therefore used the
235 nearby Tsagan-Turutuin-gol catchment as a reference, which also originates in the

236 Khangai Mountains and shares similar topographic and climatic characteristics with the
237 study basins (Klimek and Starkel, 1980). The model employed a precipitation increase
238 rate of 4.2% per 100 m and a temperature lapse rate of 0.6°C per 100 m .

239



240

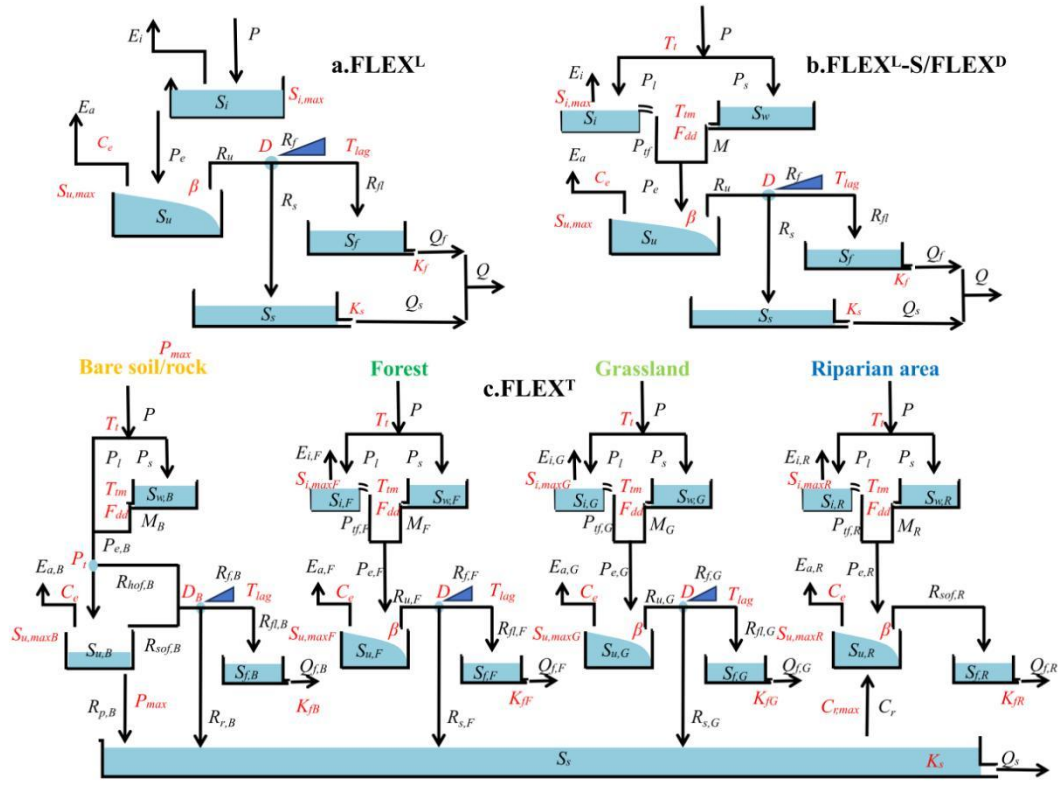
241 **Fig.2** Area of different elevation and landscape in Bogd Uliastai and Zavkhan Guulin river basins.

242

243 4. Modelling approach

244 4.1 Model description

245 To assess the impact of topography and vegetation on hydrological processes, this study
246 designed and tested four conceptual models with increasing complexity: FLEX^L,
247 FLEX^{L-S}, FLEX^D, and FLEX^T. The model structure and variables are shown in Fig.3
248 and Table 1, and the water balance, isotope mass balance and constitutive equations are
249 shown in Table 2.



250

251 **Fig.3** Stepwise modelling and the model structure of four models. (a) $FLEX^L$ is a lumped model
 252 without snow module; (b) $FLEX^L-S$ is a lumped model with snow module, and $FLEX^D$ is a semi-
 253 distributed model with the same structure as $FLEX^L-S$. (c) $FLEX^T$ is a landscape-driven semi-
 254 distributed model.

255

256 **Table1.** The variables of four models. In $FLEX^T$ model, variables associated with various landscape
 257 categories are differentiated using specific suffixes, e.g., $E_{i,F}$, represent the interception from forest.

Variables	Meaning	Variables	Meaning
P (mm/d)	Precipitation	E_i (mm/d)	Interception
S_i (mm)	Interception reservoir	P_s (mm/d)	Snowfall
P_l (mm/d)	Rainfall	P_{if} (mm/d)	Effective rainfall after interception
M (mm/d)	Snowmelt	P_e (mm/d)	Effective precipitation
S_u (mm)	Root zone reservoir	E_a (mm/d)	Actual evaporation
R_u (mm/d)	Generated runoff from the root zone reservoir	R_f (mm/d)	Generated fast runoff
R_{fl} (mm/d)	Discharge into the fast response reservoir after the convolution	R_s (mm/d)	Generated slow runoff

R_{hof} (mm/d)	Hortonian overland flow from bare soil/rock	R_p (mm/d)	Deep percolation from bare soil/rock
R_{sof} (mm/d)	Saturation overland flow	R_r (mm/d)	Water re-infiltrating
S_f (mm)	Fast response reservoir	S_s (mm)	Slow response reservoir
C_r (mm/d)	Capillary rise from groundwater into root zone reservoir on riparian area	Q_f (mm/d)	Surface flow /subsurface storm flow
Q_s (mm/d)	Groundwater flow	Q (mm/d)	Total runoff

258

259

260

261 **Table 2.** The water balance and constitutive equations used in four models. Note: FLEX^L model lacks the snow module, resulting in different water balance and
262 structural equations compared to other models. For FLEX^T model, in Eqs.7 and 9, the S_i and $S_{i,max}$ represent the interception reservoir and its interception capacity,
263 respectively, for different landscape units, including forest ($S_{i,max,F}$), grassland ($S_{i,max,G}$) and riparian area ($S_{i,max,R}$). No interception reservoir is defined for bare soil/rock
264 areas. Similarly, the S_u and $S_{u,max}$ denote the root zone reservoirs and their corresponding storage capacities for different landscapes, while K_f represents the recession
265 coefficient of the fast response reservoir for each landscape type.

Reservoirs	Water balance equations	Constitutive equations
Interception reservoir (FLEX ^L)	$\frac{dS_i}{dt} = P - E_i - P_e$ (1)	$E_i = \min(E_p, \min(P, S_{i,max}))$ (2) $P_e = \max(P - E_i, 0)$ (3)
Snow reservoir (FLEX ^L -S/FLEX ^D /FLEX ^T)	$\frac{dS_w}{dt} = P_s - M$ (4)	$P_s = \begin{cases} P; & T < T_t \\ 0; & T \geq T_t \end{cases}$ (5) $M = \begin{cases} F_{dd}(T - T_{tm}); & T > T_{tm} \\ 0; & T \leq T_{tm} \end{cases}$ (6)
Interception reservoir (FLEX ^L -S/FLEX ^D /FLEX ^T)	$\frac{dS_i}{dt} = P_l - E_i - P_{tf}$ (7)	$P_l = \begin{cases} P; & T \geq T_t \\ 0; & T < T_t \end{cases}$ (8) $E_i = \min(E_p, \min(P_l, S_{i,max}))$ (9) $P_{tf} = \max(P_l - E_i, 0)$ (10) $P_e = P_{tf} + M$ (11)

$$\frac{dS_u}{dt} = P_e - E_a - R_u \quad (12)$$

$$E_a = (E_p - E_i) \min\left(\frac{S_u}{C_e S_{u,max}}, 1\right) \quad (13)$$

$$R_u = \begin{cases} P_e - S_{u,max} + S_u + S_{u,max} \left(1 - \frac{P_e + AU}{(1+\beta)S_{u,max}}\right)^{(1+\beta)} & ; (1+\beta)S_{u,max} > P_e + AU \\ P_e - S_{u,max} + S_u & (1+\beta)S_{u,max} \leq P_e + AU \end{cases} \quad (14)$$

Root zone reservoir

(All)

$$AU = (1 + \beta)S_{u,max} \left(1 - \left(1 - \frac{S_u}{S_{u,max}}\right)^{\frac{1}{1+\beta}}\right) \quad (15)$$

$$R_f = R_u D \quad (16)$$

$$R_s = R_u(1 - D) \quad (17)$$

Splitter and lag function (All)

$$R_{f,l} = \sum_{i=1}^{T_{lag}} c(i) \cdot R_f(t - i + 1) \quad (18)$$

$$c(i) = i / \sum_{u=1}^{T_{lag}} u \quad (19)$$

$$Q_f = S_f / K_f \quad (21)$$

$$\frac{dS_f}{dt} = R_f - Q_f \quad (20)$$

Fast reservoir (All)

$$Q_s = S_s / K_s \quad (23)$$

$$\frac{dS_s}{dt} = R_s - Q_s \quad (22)$$

Slow reservoir (All)

267 4.1.1 FLEX^L

268 FLEX^L is a lumped conceptual hydrological model composed of four reservoirs
269 (Fig.3a): an interception reservoir (S_i), a root zone reservoir (S_u), a fast response
270 reservoir (S_f), and a slow response reservoir (S_s). A lag function is used to represent the
271 lag time from storm to peak flow (T_{lag}). FLEX^L includes a total of 8 free calibration
272 parameters (Table 3).

273

274 The interception reservoir was designed to simulate the process of precipitation
275 interception by vegetation canopies or the ground surface (Eq.1). Interception
276 evaporation (E_i) was calculated by potential evaporation (E_p) and S_i , considering the
277 interception storage capacity ($S_{i,max}$) (Eq.2). When precipitation (P) exceeds $S_{i,max}$, the
278 excess precipitation is routed as effective precipitation (P_e) into the root zone reservoir
279 (Eq.3).

280

281 In the root zone reservoir, actual evaporation (E_a) was estimated based on $E_p - E_i$ and
282 root zone soil moisture ($S_u/S_{u,max}$) (Eq.13). The parameter C_e represents the threshold
283 value controlling evaporation from the root zone soil moisture, and $S_{u,max}$ is root zone
284 storage capacity. The water retention curve from the Xin'anjiang model was used to
285 partition P_e into stored water in S_u and runoff generated from the root zone (R_u) (Eqs.14
286 and 15) (Zhao, 1992).

287

288 In the response reservoir, a splitter D was applied to divide the R_u into two fluxes (R_f
289 and R_s) (Eqs.16 and 17), and Eqs (18) and (19) were used to describe the lag time
290 between storm and peak flow. $R_f(t-i+1)$ represents the fast runoff generated in the root
291 zone at time $t-i+1$, T_{lag} represents the time lag between the storm and fast runoff
292 generation. $c(i)$ is the weight of the flow in $i-1$ days before and $R_f(t)$ is the discharge
293 into the fast response reservoir after convolution. We used two linear reservoirs to
294 represent the response process of subsurface storm flow (Q_f) and groundwater flow (Q_s)
295 (Eqs.21 and 23).

296

297 **4.1.2 FLEX^L-S**

298 FLEX^L-S builds upon the FLEX^L model by incorporating a snow reservoir (S_w) to
299 simulate the snow accumulation and melt processes (Fig.3b). When the daily air
300 temperature exceeds the threshold temperature (T_t) and there is no snowpack (typically
301 in summer), the interception process governs the initial partitioning of precipitation
302 (Eq.7). In contrast, when the daily mean temperature is below T_t (normally occurs in
303 winter), precipitation is stored as snow (Eq.5). When there is snowpack and the daily
304 air temperature is above T_t (normally prevailing in early spring and early autumn),
305 effective precipitation (P_e) is equal to the sum of effective rainfall after interception (P_{tf})
306 and snowmelt (M) (Eq.11). M was calculated by the snow degree day factor (F_{dd}) and
307 the threshold temperature for melting (T_{im}) (Eq.6) (Gao et al., 2017). In this study, T_{im}
308 was set to the same value as T_t . It is important to note that meltwater is conceptualized
309 as directly infiltrating into the soil, thereby bypassing the interception reservoir.

310

311 **4.1.3 FLEX^D**

312 FLEX^D is a semi-distributed model with the same structure and parameters as FLEX^L-
313 S (Fig.3b). Using DEM data, the Bogd Uliastai river basin was divided into 45 elevation
314 bands with 50 m interval, while the Zavkhan Guulin river basin was divided into 44
315 elevation bands as shown in Fig.2. The FLEX^D model was operated with semi-
316 distributed input data (see Sect.3.2), ensuring the integration of spatial variability into
317 the model's processes.

318

319 **4.1.4 FLEX^T**

320 The FLEX^T model classified the Bogd Uliastai river basin into four landscape
321 elements—bare soil/rock, forest, grassland, and riparian area—based on vegetation
322 characteristics. In contrast, the Zavkhan Guulin river basin, which has no forest, was
323 categorized into three landscape elements. By integrating both landscape types and

324 elevation bands, the Bogd Uliastai river basin was further subdivided into 132 HRUs,
325 while the Zavkhan Guulin river basin consisted of 117 HRUs (Fig.2).

326

327 The FLEX^T model's structure comprised four parallel components, representing the
328 distinct hydrological functions associated with landscape elements (Gao et al., 2014).
329 To capture the diverse rainfall-runoff processes in different landscape types, landscape
330 elements were assigned model structures (Fig.3c) and parameters (Table 3) tailored to
331 their dominant hydrological processes.

332

333 For bare soil and rock areas, vegetation is absent; therefore, no interception occurs. Due
334 to the low infiltration capacity of these surfaces, Hortonian overland flow ($R_{hof,B}$)
335 dominates runoff generation when daily effective precipitation ($P_{e,B}$) exceeds the
336 threshold parameter (P_t) (Eq. 24):

$$337 \quad R_{hof,B} = \max(P_{e,B} - P_t, 0) \quad (24)$$

338 Saturation overland flow ($R_{sof,B}$), , caused by the limited storage capacity of shallow
339 soils, occurs when the unsaturated zone soil moisture reaches its maximum storage
340 capacity ($S_{u,maxB}$). Deep percolation into groundwater ($R_{p,B}$) is governed by relative soil
341 moisture ($S_{u,B}/S_{u,maxB}$) and the maximum percolation (P_{max} ; Eq. 25). Surface runoff is
342 further partitioned into re-infiltrating water ($R_{r,B}$) over high-permeability debris slopes
343 and water routed directly to the channel ($R_{f,B}$) through a separator (D_B).

$$344 \quad R_{p,B} = P_{max} \frac{S_u}{S_{u,max}} \quad (25)$$

345

346 Forest and grassland hillslopes follow the same FLEX^D model structure, with
347 differences represented through parameters governing interception and root zone
348 processes.

349

350 For the riparian area, which is prone to saturation due to its location, we also constrained
351 a shallower $S_{u,maxR}$, with the effect of capillary rise (C_r) taken into account. C_r is
352 represented by a parameter ($C_{r,max}$) indicating a constant amount of capillary rise. The

353 lag time from storm to peak flow was not considered in riparian area.

354

355 Interception thresholds were parameterized to be highest for forest ($S_{i,maxF}$), followed
356 by grassland ($S_{i,maxG}$) and riparian area ($S_{i,maxR}$), reflecting differences in canopy
357 interception capacity.

358 The root zone storage capacity was assigned deepest in forests ($S_{u,maxF}$), shallower in
359 grasslands ($S_{u,maxG}$), and smallest in riparian areas ($S_{u,maxR}$). Bare soil and rock ($S_{u,maxB}$)
360 were represented as belonging to the unsaturated zone rather than the root zone, with
361 storage capacity similar to that of riparian areas. Response timescales were
362 parameterized to be longest for groundwater (K_s), shortest for saturation-excess runoff
363 in riparian area (K_{fR}) and surface runoff in bare soil/rock (K_{fB}), with subsurface flow
364 from forest and grassland (K_{fF} and K_{fG}) parameterized to operate at intermediate
365 timescales.

Table 3. Uniform prior parameter distributions of four models.

Models	Parameter	Explanation	Prior range
	$S_{i,max}$ (mm)	Storage capacity of interception reservoir	(0.1, 2)
	$S_{u,max}$ (mm)	Root zone storage capacity	(5, 300)
	K_f (d)	Recession coefficient of fast response reservoir	(1, 10)
	C_e (-)	Threshold controls actual evaporation and transpiration	(0, 1)
FLEX ^L	β (-)	Shape parameter of the tension water storage capacity curve	(0.1, 5)
	D (-)	Splitter between fast runoff and slow recharge	(0, 1)
FLEX ^D	T_{lag} (-)	Time lag between storm and fast runoff generation	(0.8, 3)
FLEX ^{L-S}	K_s (d)	Recession coefficient of slow response reservoir	(10, 200)
	T_i (°C)	Threshold temperature to split snowfall and rainfall	(-2, 2)
FLEX ^T	T_{im} (°C)	Threshold temperature for melting	(-2, 2)
	F_{dd} (mm(°Cd) ⁻¹)	Snow degree day factor	(1, 6)
	P_t (mm/d)	Infiltration threshold for initiating Hortonian overland flow	(5, 35)
	P_{max} (mm/d)	Maximum percolation	(0.1, 5)
	D_B (-)	splitter between fast surface runoff and re-infiltration	(0, 1)
	$S_{i,max,F}$ (mm)	Interception storage capacity of forest	(0.5, 2)

$S_{i,maxG}$ (mm)	Interception storage capacity of grassland	(0.1, 1)
$S_{i,maxR}$ (mm)	Interception storage capacity of riparian area	(0.1, 1)
$S_{u,maxB}$ (mm)	Unsaturated storage capacity of bare soil/rock	(5, 120)
$S_{u,maxF}$ (mm)	Root zone storage capacity of forest	(50, 300)
$S_{u,maxG}$ (mm)	Root zone storage capacity of grassland	(10, 300)
$S_{u,maxR}$ (mm)	Root zone storage capacity of riparian area	(5, 120)
K_{fB} (d)	Recession coefficient of the fast response reservoir for bare soil/rock	(1, 5)
K_{fF} (d)	Recession coefficient of the fast response reservoir for forest	(1, 10)
K_{fG} (d)	Recession coefficient of the fast response reservoir for grassland	(1, 10)
K_{fR} (d)	Recession coefficient of the fast response reservoir for riparian area	(1, 5)
C_{Rmax} (mm/d)	Constant amount of capillary rise	(0.1, 2)

368 **4.2 The ratio of snowmelt runoff to streamflow**

369 This study quantifies the ratio of snowmelt runoff to streamflow using the FLEX^T
370 model. The model assumes that snowmelt and rainfall mix rapidly and completely upon
371 entering the model's conceptual reservoirs, thereby altering its internal composition
372 ratios. The composition ratio of the water exiting the reservoir is identical to that within
373 the reservoir (Liu et al., 2023). The method enables the tracking of ratio of snowmelt
374 runoff to streamflow ($f_{Q,snow}$) at each time step by the following equation:

$$375 \quad f_{Q,snow} = \frac{Q_M}{Q} = \frac{Q_{f,M} + Q_{s,M}}{Q} \quad (26)$$

$$376 \quad Q_{f,M} = \frac{\left(\frac{M}{P_e}\right)S_f}{K_f} \quad (27)$$

$$377 \quad Q_{s,M} = \frac{\left(\frac{M}{P_e}\right)S_s}{K_s} \quad (28)$$

378 where Q is total runoff in the river channel; Q_M is snowmelt runoff in the river channel;
379 $Q_{f,M}$ is surface flow or subsurface storm flow generated by snowmelt; $Q_{s,M}$ is
380 groundwater flow generated by snowmelt.

381

382 **4.3 Model calibration and uncertainty estimation**

383 For the Bogd Uliastai river basin, the model was warmed up using data from 2007,
384 calibrated during 2008–2011, and validated during 2012–2015. For the Zavkhan Guulin
385 river basin, 2000 was used as the warm-up year, with 2001–2010 selected for
386 calibration and 2011–2020 for validation.

387

388 The MOSCEM-UA (Multi-objective Shuffled Complex Evolution Metropolis
389 Algorithm) integrates multi-objective optimization and Bayesian uncertainty analysis,
390 featuring global search capabilities that facilitate the generation of multiple Pareto
391 optimal solutions and provide an assessment of uncertainty (Vrugt et al., 2003). The
392 MOSCEM-UA was run for the optimization of parameters, with 40000 iterations for
393 each of the four model structures. The model parameters and their prior ranges for
394 calibration are listed in Table 3.

395

396 The Kling-Gupta Efficiency (KGE) and its logarithmic form (KGL) were used as
 397 objective functions to evaluate the simulation of daily discharge (Gupta et al., 2009).
 398 These two metrics were chosen because each emphasizes a different portion of the
 399 hydrograph: KGE is more sensitive to high-flow dynamics, while KGL better captures
 400 low-flow conditions. In this study, to accommodate minimization-based optimization
 401 algorithms, the runoff objective functions L_1 (Eq.29) and L_2 (Eq.30) were formulated
 402 as one minus their respective efficiency metrics. The two objective functions were
 403 assigned equal weights during model calibration to ensure a balanced representation of
 404 both high- and low-flow regimes.

$$405 \quad L_1 = 1 - KGE = \sqrt{(1 - \gamma)^2 + (1 - \alpha)^2 + (1 - \beta)^2} \quad (29)$$

$$406 \quad L_2 = 1 - KGL = \sqrt{(1 - \gamma_{log})^2 + (1 - \alpha_{log})^2 + (1 - \beta_{log})^2} \quad (30)$$

407 where, γ is the correlation coefficient between simulated and observed flows, and γ_{log} is
 408 the correlation coefficient between their logarithmic values; α is the ratio of the standard
 409 deviations of the simulated and observed flows, and α_{log} is the ratio of the standard
 410 deviations of their logarithmic transformations; β is the ratio of the mean values of the
 411 simulated and observed flows, and β_{log} is the ratio of the mean values of their
 412 logarithmic transformations.

413 **5. Results**

414 **5.1 Model calibration and validation**

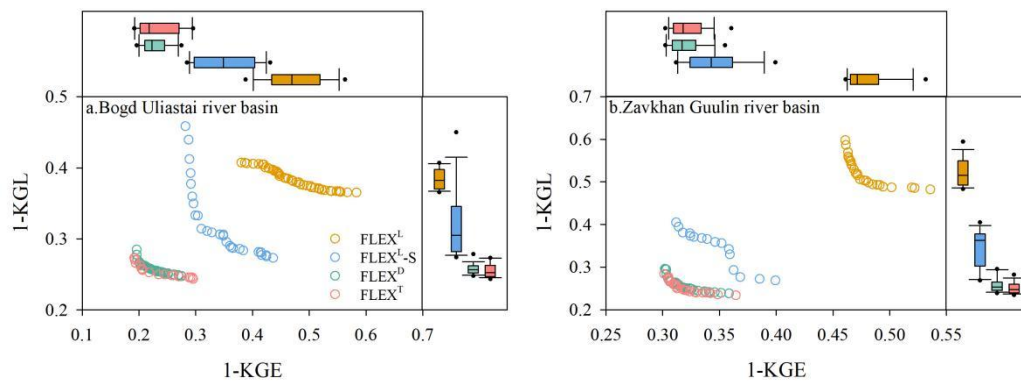
415 Fig.4 shows the performance of the four models during the calibration period. The
 416 Pareto-optimal front shifts progressively toward the origin, indicating that model
 417 structural modifications enhance the model's ability to capture basin runoff dynamics.
 418 The FLEX^L-S model (KGE: 0.65 and 0.65, with the former representing the Bogd
 419 Uliastai river basin and the latter representing the Zavkhan Guulin river basin,
 420 hereinafter referred to as the same; KGL: 0.68 and 0.66) outperforms the baseline
 421 FLEX^L model (KGE: 0.53 and 0.52; KGL: 0.62 and 0.48) (Table 4). This improvement
 422 highlights the importance of explicitly representing snow processes in cryospheric
 423 regions. Without accounting for snow accumulation and ablation, the model tends to

424 overestimate small peak flow events in winter, as shown in Fig.5, underscoring the
425 critical role of snow dynamics in shaping hydrological responses.

426

427 The FLEX^D model (KGE: 0.77 and 0.68; KGL: 0.74 and 0.74) outperforms the FLEX^L-
428 S, with the distributed precipitation and temperature inputs significantly improving the
429 simulation of peak flow. FLEX^D does not require a more complex model structure or
430 additional parameters compared to FLEX^L-S. For hydrograph simulation, FLEX^T (KGE:
431 0.78 and 0.68; KGL: 0.75 and 0.75) performs comparably to FLEX^D.

432



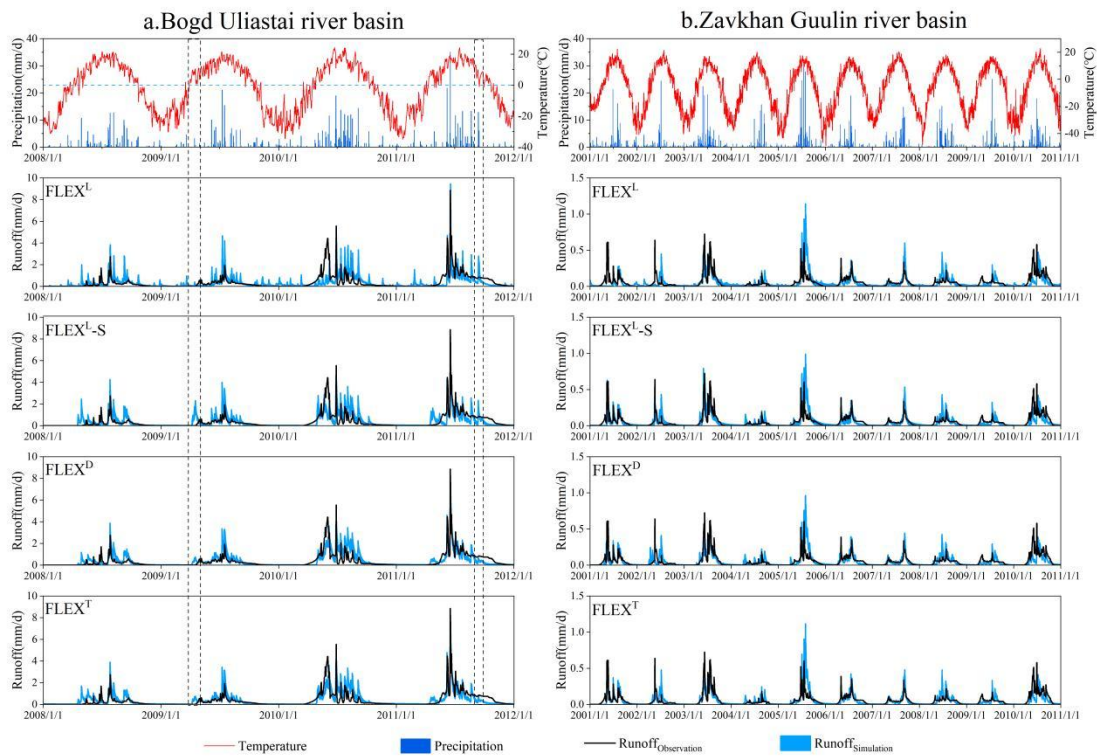
433

434 **Fig.4** Performance of the FLEX^L, FLEX^L-S, FLEX^D, and FLEX^T models during the calibration
435 period.

Table 4 Comparison of simulation performance among different hydrological models in the two study catchments.

Basins	Evaluation indicators	Calibration					Validation						
		FLEX ^L	FLEX ^{L-S}	FLEX ^D	FLEX ^T	FLEX ^L	FLEX ^{L-S}	FLEX ^D	FLEX ^T	FLEX ^L	FLEX ^{L-S}	FLEX ^D	FLEX ^T
Bogd Uliastai river basin	Max	0.62	0.72	0.80	0.81	0.58	0.63	0.62	0.63	0.63	0.62	0.63	0.63
	Median	0.53	0.65	0.77	0.78	0.39	0.47	0.56	0.59	0.56	0.56	0.59	0.59
	Min	0.42	0.56	0.73	0.70	0.16	0.29	0.52	0.51	0.52	0.52	0.51	0.51
	Max	0.63	0.73	0.75	0.76	0.67	0.76	0.80	0.81	0.80	0.80	0.81	0.81
	Median	0.62	0.68	0.74	0.75	0.64	0.71	0.78	0.78	0.78	0.78	0.78	0.78
	Min	0.59	0.54	0.72	0.73	0.61	0.61	0.75	0.75	0.75	0.75	0.75	0.75
Zavkhan Guulin river basin	Max	0.54	0.69	0.70	0.70	0.41	0.59	0.62	0.63	0.62	0.62	0.63	0.63
	Median	0.52	0.65	0.68	0.68	0.31	0.47	0.56	0.59	0.56	0.56	0.59	0.59
	Min	0.46	0.60	0.64	0.64	0.13	0.28	0.41	0.52	0.41	0.41	0.52	0.52
	Max	0.52	0.73	0.76	0.77	0.60	0.73	0.74	0.74	0.74	0.74	0.74	0.74
	Median	0.48	0.66	0.74	0.75	0.56	0.66	0.72	0.73	0.72	0.72	0.73	0.73
	Min	0.40	0.60	0.70	0.72	0.47	0.61	0.70	0.71	0.70	0.70	0.71	0.71

438 Some interesting rain/snowmelt-runoff events also suggest that semi-distributed models
 439 (FLEX^D and FLEX^T) better capture basin hydrological processes. Two such events in
 440 the Bogd Uliastai river basin in April 2009 and September 2011 provide compelling
 441 evidence (Fig.5). On 14 April 2009, despite minimal precipitation, temperatures
 442 exceeded the melting threshold, producing only a relatively insignificant peak flow. In
 443 12 September 2011, despite a higher daily precipitation of 12.7 mm, no runoff peak was
 444 observed within the basin. Lumped models failed to reproduce these dynamics
 445 accurately, instead simulating much larger peak flows.
 446

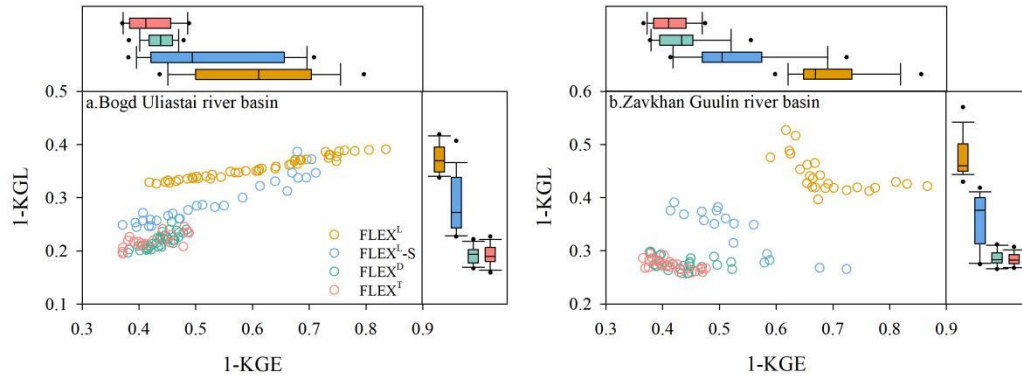


447
 448 **Fig.5** The daily observed and simulated hydrographs of the FLEX^L, FLEX^{L-S}, FLEX^D, and FLEX^T
 449 models in the calibration period. The dashed boxes represent the rainfall/snowfall-runoff events on
 450 14 April 2009 and 12 September 2011 in the Bogd Uliastai river basin.

451
 452 The performance and results of the four models during the validation period are shown
 453 in Figs.6 and 7. The results confirm the stepwise improvement in model performance,
 454 as evidenced by the points corresponding to different model structures progressively
 455 shifting toward the origin. With the gradual optimization of model structure, the

456 model's fitness has significantly improved. Unlike during calibration, the points in the
 457 validation period do not maintain the arc shape (Fig.4).

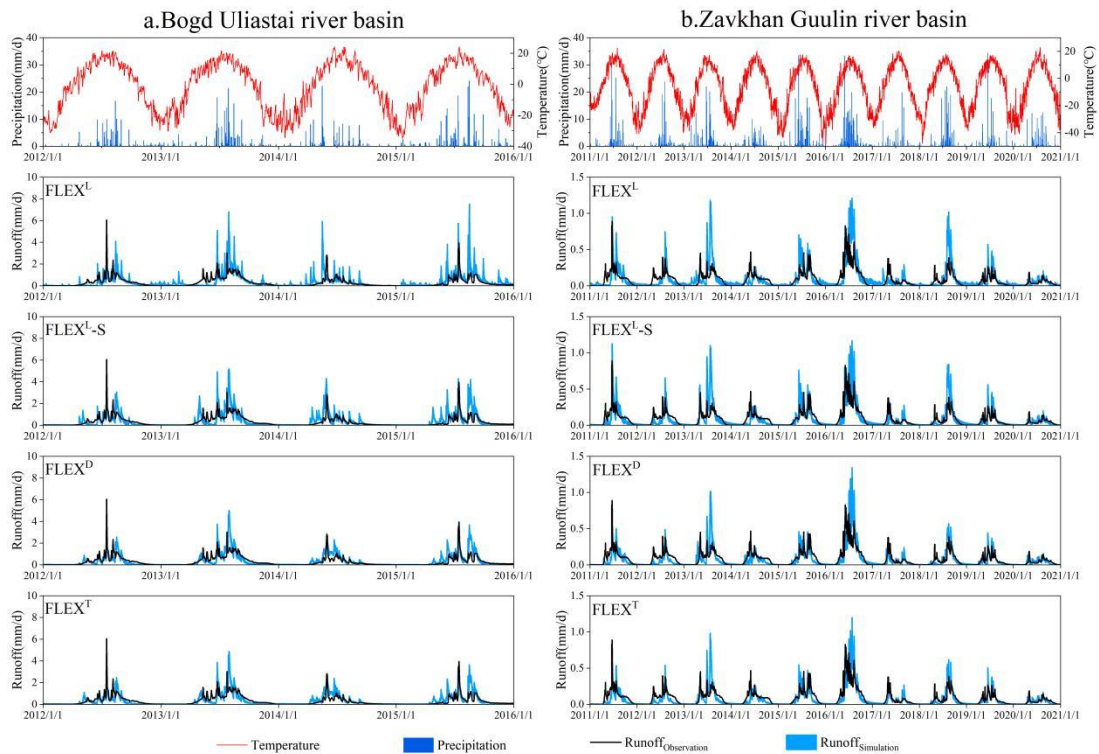
458



459

460 **Fig.6** Performance of the $FLEX^L$, $FLEX^{L-S}$, $FLEX^D$, and $FLEX^T$ models in validation mode.

461



462

463 **Fig.7** The daily observed and simulated hydrographs of the $FLEX^L$, $FLEX^{L-S}$, $FLEX^D$, and $FLEX^T$
 464 models in the validation period.

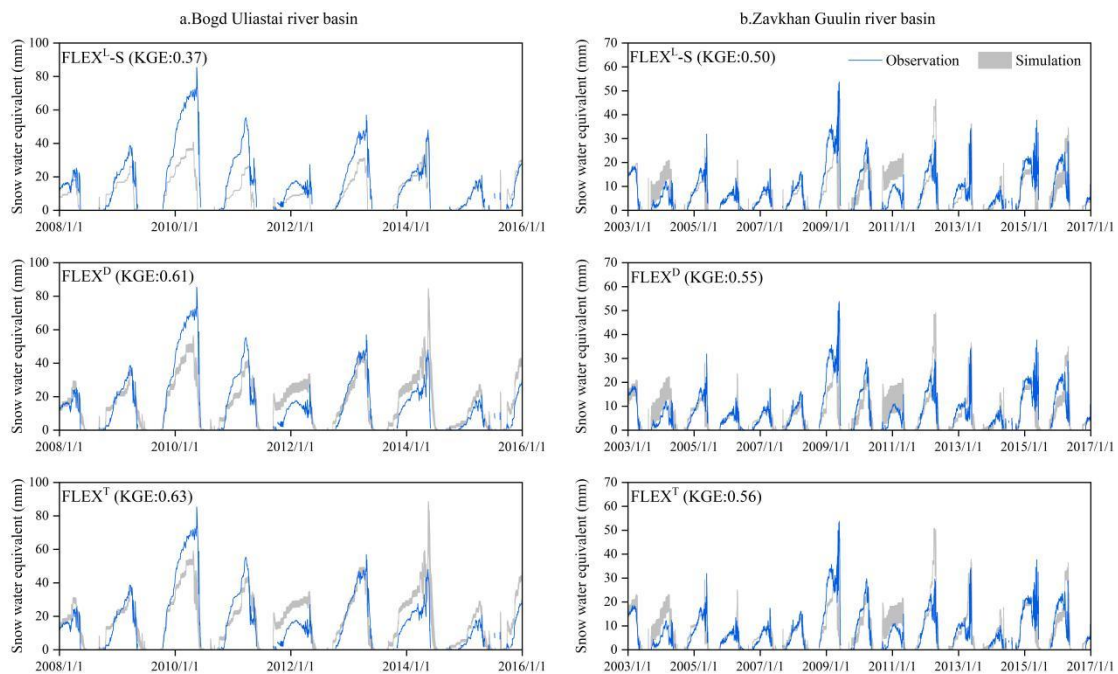
465

466 5.2 Model test by snowpack dynamics

467 Snow water equivalent is a crucial indicator of snowmelt dynamics and plays an

468 essential role in hydrological modelling, serving as an additional metric for evaluating
 469 model performance and realism (Fig.8). In the Bogd Uliastai river basin, the FLEX^D
 470 and FLEX^T models achieved KGE values of 0.61 and 0.63, respectively, for SWE
 471 simulation, indicating their ability to capture seasonal patterns and interannual
 472 variability, particularly peak values during winter and spring. The FLEX^{L-S} model, which
 473 incorporates vegetation effects, further improved SWE simulation accuracy and
 474 enhanced responsiveness to hydrological processes. In contrast, the FLEX^{L-S} model
 475 yielded a KGE of only 0.37, reflecting its limitations in capturing snowpack dynamics
 476 within the basin.

477



478

479 **Fig.8** The observed and simulated daily snow water equivalent of the FLEX^{L-S}, FLEX^D, and FLEX^T
 480 models.

481

482 In the Zavkhan Guulin river basin, the FLEX^{L-S} model demonstrated relatively stable
 483 performance, achieving a KGE of 0.50. Although lumped models struggle to capture
 484 spatial heterogeneity, they effectively reflect seasonal precipitation and snowmelt
 485 trends. FLEX^D and FLEX^T achieved KGE values of 0.55 and 0.56, respectively, showed
 486 slight improvements. Overall, the semi-distributed model exhibited consistently higher
 487 SWE simulation skill across both basins.

488

489 **5.3 Model parameters composition**

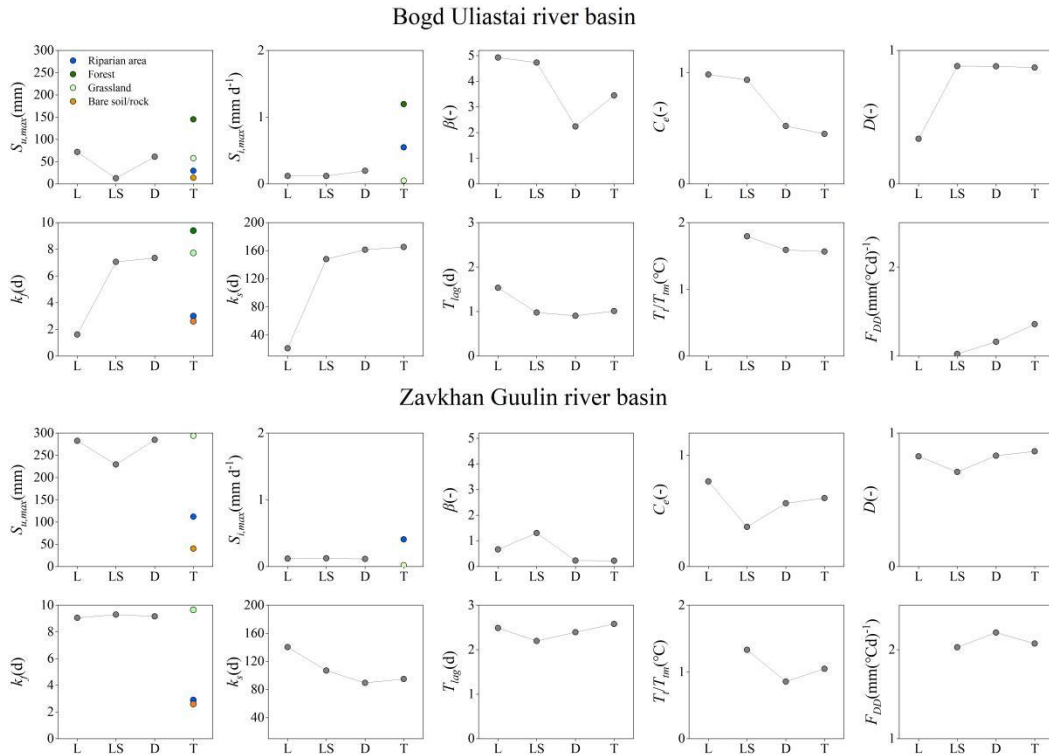
490 Fig.9 shows that model parameters exhibit distinct sensitivity across different structural
491 configurations within the stepwise modelling framework. In models that do not account
492 for vegetation effects, single parameter values are used to approximate basin-average
493 hydrological behavior, whereas FLEX^T produces spatially differentiated parameter
494 values across landscape units.

495

496 Interception capacity ($S_{i,max}$) and root zone storage capacity ($S_{u,max}$) vary across
497 landscapes. In the Bogd Uliastai river basin, forest (present only in this basin) shows
498 the highest $S_{i,max}$ (1.19 mm), followed by riparian area (0.55 mm) and grassland (0.05
499 mm), while bare soil/rock has no interception storage. $S_{u,max}$ decreases from forest (145
500 mm) to grassland (54 mm), riparian area (29 mm), and bare soil/rock (14 mm). By
501 comparison, in the Zavkhan Guulin river basin, $S_{i,max}$ is lower (grassland: 0.02 mm;
502 riparian area: 0.41 mm), whereas $S_{u,max}$ is higher (grassland: 283 mm; riparian area: 105
503 mm; bare soil/rock: 33 mm), reflecting the more arid conditions and associated
504 hydrological characteristics.

505

506 The recession coefficient of the fast response reservoir (K_f) reflects runoff dynamics
507 and storage across landscapes. In the Bogd Uliastai river basin, forest has the largest K_f
508 (9.4 d), followed by grassland (7.7 d), while riparian areas (3.0 d) and bare soil/rock
509 (2.6 d) have the smallest K_f , indicating faster runoff. In the Zavkhan Guulin river basin,
510 K_f shows a similar pattern, with grassland (9.7 d), riparian areas (2.9 d), and bare
511 soil/rock (2.5 d). The low K_f in bare soil/rock reflects Hortonian overland flow, whereas
512 runoff in riparian areas is mainly governed by saturation overland flow.



513

514 **Fig.9** The changes of averaged behavioral parameters of the FLEX^L, FLEX^{L-S}, FLEX^D, and FLEX^T
 515 models.

516

517 Other parameters are also refined alongside improvements in the model structure. The
 518 parameter D , which partitions generated runoff between fast and slow response
 519 reservoirs, tends to be close to 1—indicating that most runoff is routed to the fast
 520 reservoir. Parameters related to energy processes, such as the T_{tm} and F_{dd} , exhibit a clear
 521 compensatory relationship: a higher T_{tm} is typically associated with a lower F_{dd} , and
 522 vice versa.

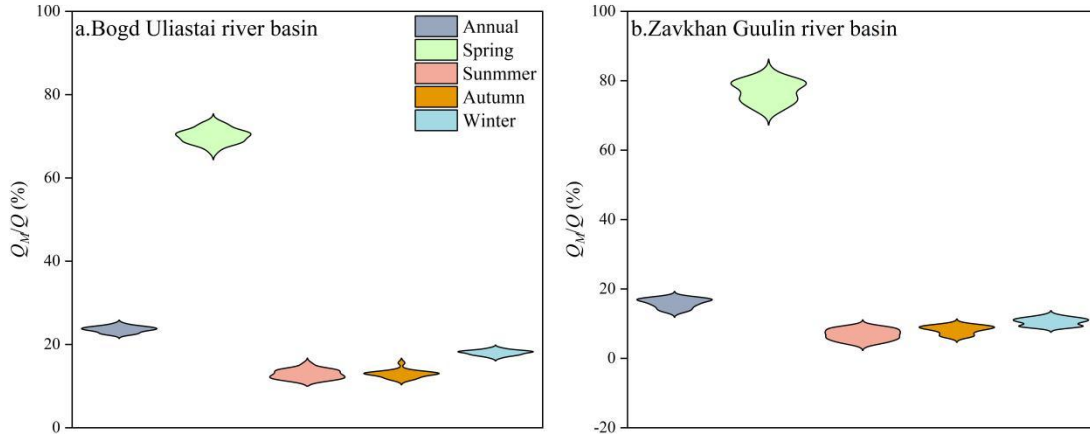
523

524 **5.4 The ratio of snowmelt runoff to streamflow**

525 Fig.10 shows the annual and seasonal ratios of snowmelt runoff to streamflow in the
 526 Bogd Uliastai and Zavkhan Guulin river basins, as simulated by the FLEX^T model. On
 527 an annual scale, snowmelt runoff accounts for 23.6%±0.7% and 15.9%±1.3% of
 528 streamflow in the Bogd Uliastai and Zavkhan Guulin river basins, respectively.
 529 Seasonally, snowmelt plays a dominant role in sustaining spring flows, with snowmelt

530 runoff accounting for $70.1\% \pm 1.7\%$ and $76.9\% \pm 3.2\%$ of streamflow in the two basins,
 531 while its contribution is considerably lower in other seasons.

532



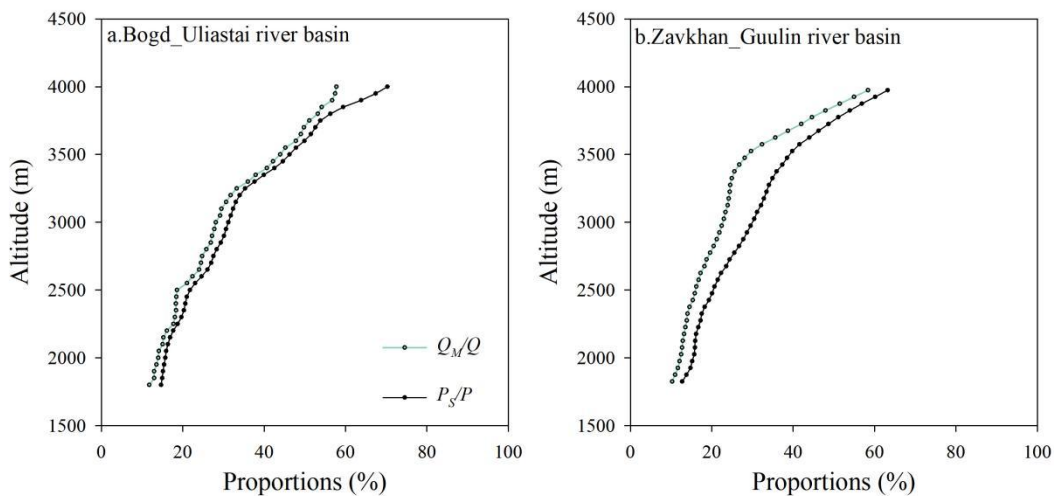
533

534 **Fig.10** The ratio of snowmelt runoff to streamflow based on the FLEX^T model.

535

536 Fig.11 shows the snowfall-to-precipitation ratio (P_s/P) and the ratio of snowmelt runoff
 537 to streamflow (Q_M/Q) across different elevations. The P_s/P increases with elevation
 538 ranging from 14.7% to 70.3% in the Bogd Uliastai river basin and from 12.7% to 63.2%
 539 in the Zavkhan Guulin river basin. Consistent with this pattern, the Q_M/Q also increases
 540 with elevation, from 11.8% to 57.8% and from 10.3% to 58.4% in the two basins,
 541 respectively. Overall, higher P_s/P are associated with higher Q_M/Q across elevations.

542



543

544 **Fig.11** The ratio of snowmelt runoff to streamflow and the snowfall-to-precipitation ratio at different

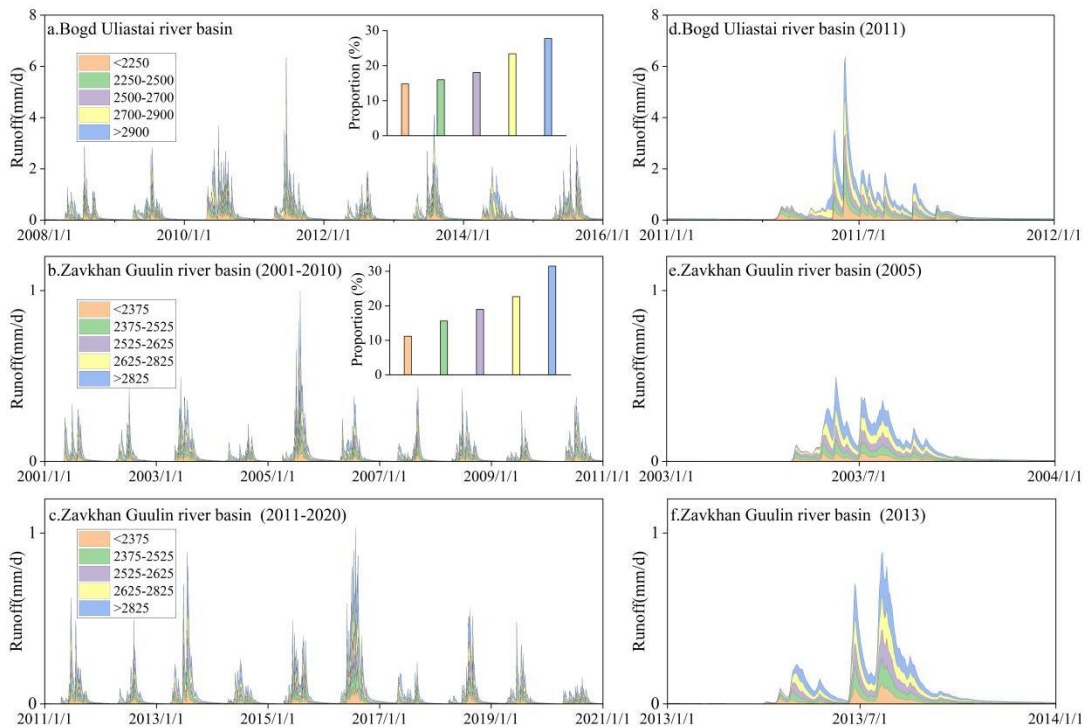
545 elevations based on FLEX^T model.

546

547 **5.5 Runoff generation at different elevations and across landscapes**

548 Fig.12 shows significant differences in runoff contributions across 5 equal area
549 elevation bands. In the Bogd Uliastai and Zavkhan Guulin river basins, high elevation
550 areas (above 2900 m in the Bogd Uliastai basin and 2825 m in the Zavkhan Guulin
551 basin) play a dominant role in runoff generation, contributing approximately 30% of
552 total basin runoff. This dominance is primarily attributed to orographic effect, which
553 increase precipitation and enhance the proportion of snowmelt-derived runoff (Fig.11).
554 In contrast, low elevation areas rely primarily on rainfall-induced runoff. Due to limited
555 precipitation and higher evaporative losses, their contributions to total runoff are
556 comparatively smaller, with the lowest elevation band accounting for only about 15%
557 of basin runoff.

558



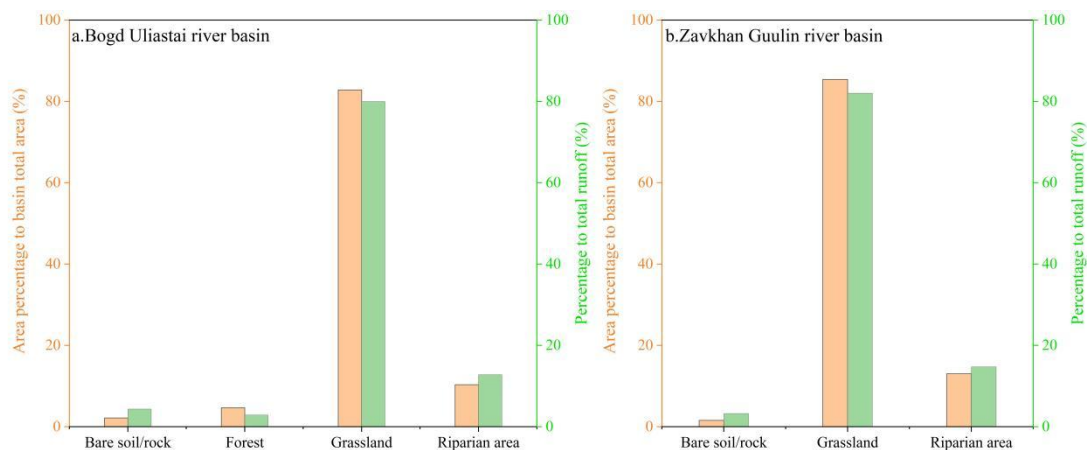
559

560 **Fig.12** Runoff contribution from 5 equal area elevation bands (each representing 20% of the total
561 catchment area) based on FLEX^T model.

562

563 Different landscape units also exhibit differences in their contributions to runoff (Fig.
 564 13). Grasslands occupy the largest portion of both basins (82.8% and 85.4% in the Bogd
 565 Uliastai and Zavkhan Guulin river basins, respectively) and contribute correspondingly
 566 high shares of total runoff (80.0% and 82.0%). Forested areas, found only in the Bogd
 567 Uliastai basin, account for 4.7% of the basin area but contribute only 2.9% of the total
 568 runoff. Riparian areas occupy a relatively small fraction of the two basins (10.3% and
 569 13.0%) but contribute a comparable or higher proportion of runoff (12.8% and 14.7%).
 570 Bare soil/rock areas generate a relatively high runoff contribution per unit area;
 571 however, their limited spatial extent (2.2% and 1.6%) constrains their total contribution
 572 to streamflow (4.3% and 3.3%).

573



574

575 **Fig.13** Runoff contribution from different landscapes based on FLEX^T model.

576

577 **6. Discussion**

578 **6.1 The stepwise modelling framework improves the simulation of** 579 **hydrological processes in cold regions**

580 Accurately representing dominant hydrological processes and spatial heterogeneity is
 581 essential for simulating runoff dynamics in cold regions. The enhanced performance of
 582 FLEX^L-S relative to the FLEX^L model underscores the necessity of explicitly
 583 representing snow accumulation and melt, which are integral to runoff generation in
 584 cryospheric environments. Without such representation, winter runoff responses tend

585 to be systematically mischaracterized.

586

587 The better performance of the distributed FLEX^D model highlights the importance of
588 elevation-dependent variability in temperature and precipitation (Fenicia et al., 2008b).

589 By maintaining distinct storage states across hydrological response units, FLEX^D
590 captures spatial contrasts in precipitation phase and melt timing that lumped models fail
591 to resolve, particularly during rain–snow transition events (Bormann et al., 2009).

592

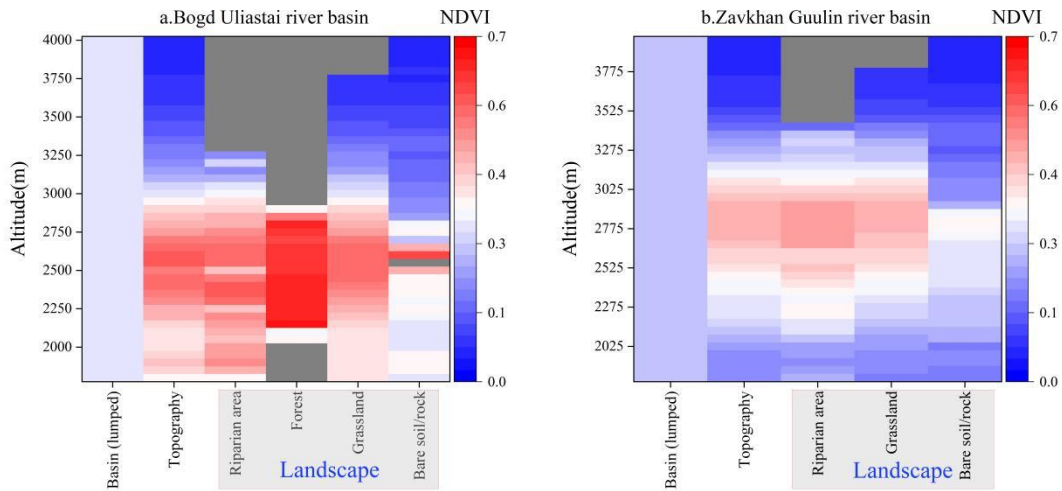
593 FLEX^T systematically integrates topography, vegetation, and hydrological processes
594 through the explicit representation of hydrological response units, thereby enhancing
595 the physical consistency of the model structure and the interpretability of its parameters
596 (Savenije, 2010). Under the basin conditions considered in this study, FLEX^T exhibits
597 a high degree of consistency with FLEX^D in simulating both runoff and snowpack
598 dynamics. Although process-based discretization approaches have been shown to
599 improve basin-scale hydrological simulations in heterogeneous cold region basins—
600 such as the Heihe (Gao et al., 2014) and Yigong Zangbu river basins (Gao et al.,
601 2020)—when topographic and land-cover variability are explicitly represented, the
602 magnitude of these benefits appears to depend strongly on the degree of landscape
603 heterogeneity.

604

605 In the studied basins, vegetation heterogeneity is limited, with grasslands covering
606 more than 80% of the area (Fig.13), which substantially reduces contrasts in vegetation
607 properties across the landscape. Although the lumped model applies a spatially uniform
608 NDVI and therefore cannot explicitly resolve intra-basin vegetation variability, NDVI
609 exhibits a strong correspondence with elevation, particularly in grassland-dominated
610 regions. NDVI values across elevation bands closely resemble those of the
611 corresponding grassland zones, indicating that vegetation distribution is largely
612 structured by topographic gradients. While forested and bare land areas display distinct

613 NDVI signatures, they occupy only a minor fraction of the basin and exert a limited
614 influence on overall runoff generation (Fig.14).

615



616

617 **Fig.14** Multi-year average NDVI variation across landscapes and its relationship with elevation in
618 two study basins.

619

620 Under these conditions, key vegetation-related hydrological attributes—such as root
621 zone storage and interception capacity — can be effectively represented through
622 hydroclimatic conditions and topographic gradients (Antonelli et al., 2018; Roebroek
623 et al., 2020), allowing elevation to function, to some extent, as a proxy for vegetation
624 structure. Consequently, the comparable performance of FLEX^T and FLEX^D in
625 simulating runoff and snowpack processes primarily reflects the constraining influence
626 of landscape structure in the studied basins, rather than differences in model design.
627 Within this stepwise modelling framework, FLEX^T employs a more physically
628 grounded parameterization scheme and therefore offers a flexible and extensible
629 platform for diagnosing hydrological processes in cold mountainous regions. This
630 suggests a particular advantage for exploring hydrological responses to vegetation and
631 climate change in basins with higher ecological or topographic complexity.

632

633 **6.2 Process-based tracking of the ratio of snowmelt runoff to**

634 **streamflow**

635 Although direct observational data (e.g., stable water isotopes) for quantifying the ratio
636 of snowmelt runoff to streamflow are unavailable in this study, previous research
637 provides indirect support. Wu et al. (2021) applied a similar snowmelt tracking method
638 in the Altai Mountain and reported that snowmelt accounted for 29.3% of annual
639 streamflow. This result exceeds those observed in our study, largely due to regional
640 differences in snowfall. In the Kayiertesu river basin of the Altai Mountain, annual
641 average precipitation for one hydrological year (September to August) was 409.8 mm
642 from 2011 to 2015 (observed at the Kuwei snow station), with snowfall from November
643 to March comprising about 31% of that annual precipitation (Zhang et al., 2017). In
644 contrast, annual precipitation in the Bogd Uliastai and Zavkhan Guulin basins does not
645 exceed 200 mm, and snowfall represents less than 15% of the total observed
646 precipitation.

647

648 This study also compared model-based snowmelt tracking with traditional indirect
649 methods, which estimate the ratio of snowmelt runoff to streamflow by calculating the
650 ratio of snowfall or snowmelt to runoff over a given period (Barnett et al., 2005;
651 Immerzeel et al., 2010). While these indirect approaches are computationally efficient
652 and require limited data, they implicitly assume that all meltwater is instantaneously
653 converted to runoff, neglecting interactions with rainfall and losses due to infiltration,
654 evaporation, and subsurface storage (Li et al., 2017).

655

656 Using the traditional indirect approach, we calculated snowmelt-to-runoff ratios of
657 $41.3\% \pm 1.6\%$ and $153\% \pm 15.5\%$ in the two basins, respectively. These estimates are
658 substantially higher than those obtained from model-based snowmelt tracking, with
659 some values exceeding 100%, indicating physical implausibility. This discrepancy
660 highlights the methodological limitations of traditional approaches.

661

662 The overestimation inherent in traditional methods arises from their failure to represent

663 snowmelt that infiltrates into the soil profile, percolates to deeper layers, or is lost
664 through evaporation, thereby reducing the fraction of meltwater reaching the channel
665 (Liu et al., 2023), particularly in the arid Zavkhan Guulin river basin. These findings
666 underscore the importance of using physically based models to trace water source
667 pathways, particularly in data-scarce and hydrologically complex regions.

668

669 **6.3 Runoff generation mechanisms at different elevations and across** 670 **landscapes**

671 Elevation is a fundamental control on runoff generation and seasonal hydrological
672 variability in mountainous basins, as it governs precipitation phase, snow accumulation,
673 and melt timing (Jenicek and Ledvinka, 2020). In the study basins, runoff contributions
674 increase progressively with elevation. This pattern contrasts with glacierized
675 catchments, where the largest runoff contributions do not necessarily originate from the
676 highest elevation bands but are often dominated by glacier melt processes (Gao et al.,
677 2020). These elevation-dependent contrasts highlight the importance of explicitly
678 accounting for vertical heterogeneity and basin-specific cryospheric conditions in cold-
679 region hydrological modelling.

680

681 The lag effect in snowmelt runoff across different elevations is a defining feature of
682 hydrological processes in mountainous basins, arising from the temporal variability of
683 snowmelt among elevation areas. In the Bogd Uliastai and Zavkhan Guulin river basins,
684 low elevation areas contribute rapidly to runoff during the initial stages, while high
685 elevation areas gradually augment runoff as the season progresses, reflecting the
686 delayed response of snowmelt-dominated areas (Hajika et al., 2024). This lag is
687 primarily governed by elevation-dependent snow accumulation and melt dynamics:
688 under cold conditions at higher elevations, precipitation is stored as snow, and
689 meltwater release typically occurs several weeks to a few months later than at lower
690 elevations, with the lag being most pronounced at the onset of the melt season (Gillan
691 et al., 2010) (Fig.12).

692

693 The lag in snowmelt runoff across different elevations has profound implications for
694 water resources management. Snowmelt from high elevation areas prolongs the
695 recession of basin runoff, maintaining downstream water supply and providing
696 buffering capacity during droughts or low-flow periods. In contrast, low elevation areas
697 respond rapidly to extreme precipitation, generating short-term flood peaks, while
698 delayed high elevation snowmelt can extend high flow conditions, complicating flood
699 management (Gu et al., 2023). Effective management in mountainous basins therefore
700 requires integrating both immediate and delayed runoff contributions across elevations
701 to optimize water allocation, improve flood early-warning accuracy, and safeguard
702 downstream ecological and socio-economic water demands (Li et al., 2019).

703

704 Beyond elevation controls, vegetation influences runoff generation through its direct
705 physiological properties (e.g., interception and root zone storage). Grasslands are the
706 dominant land-cover type in both basins and are widely distributed across different
707 elevation zones. Their runoff-generation characteristics are relatively spatially uniform
708 in a basin-averaged sense and thus exert a primary control on the overall runoff response.
709 Under the semi-arid and arid climatic setting, soils in grassland areas are generally
710 persistently dry, with a large initial soil-moisture deficit. This condition thereby
711 enhances the infiltration demand for rainfall and snowmelt, delaying runoff generation
712 (Xue et al., 2025). Forested areas exhibit strong regulatory functions—intercepting
713 precipitation, enhancing infiltration, and reducing quick flow generation (Liu et al.,
714 2018; Stocker et al., 2023). Riparian areas function as hydrologically connected source
715 areas, rapidly transmitting rainfall and snowmelt to the channel network (Leibowitz et
716 al., 2023). The runoff generation capacity of bare soil/rock is high due to the lack of
717 vegetation and low soil permeability. After rainfall or snowmelt, water infiltrates poorly
718 and rapidly forms overland flow (Zeng et al., 2024). Although their basin-scale
719 contribution is constrained by areal extent, these surfaces can locally intensify runoff
720 responses and sediment transport.

721

722 These findings support the view that vegetation functions as a spatially variable
723 regulator of runoff generation. This regulatory effect is particularly sensitive to future
724 changes in vegetation cover and distribution under climate and land use change
725 scenarios. For instance, overgrazing may reduce aboveground biomass and root zone
726 storage capacity, thereby increasing runoff and erosion risks (Donovan and Monaghan,
727 2021), while shifts in vegetation type (e.g., shrub encroachment or forest decline) could
728 alter hydrological partitioning along elevation gradients (Hsu et al., 2025; Zhou et al.,
729 2023).

730

731 **6.4 Applicability and limitations of the modelling framework**

732 Previous applications of the FLEX framework in alpine basins, such as the Heihe river
733 basin, provide an important reference for interpreting the results of this study. In the
734 Heihe river basin, FLEX^T was configured using terrain-driven functional units,
735 whereby the catchment was discretized into four topographic sub-units representing
736 distinct dominant hydrological processes. This modelling strategy primarily focused on
737 assessing model realism and transferability across sub-basins by demonstrating the
738 ability of FLEX^T to reproduce contrasting functional hydrological behaviors (Gao et al.,
739 2014). Building on these earlier studies, the present work further demonstrates that the
740 FLEX framework can also be adapted to colder and more semi-arid conditions using a
741 stepwise strategy. Importantly, our emphasis extends beyond discharge performance to
742 diagnosing runoff-generation mechanisms—specifically the snowmelt contribution to
743 streamflow and the relative roles of elevation bands and vegetation units—thereby
744 clarifying how topography and land cover jointly shape hydrological responses in cold
745 alpine basins.

746

747 While the proposed modelling framework captures key hydrological processes, several
748 limitations should be acknowledged. First, frozen soil processes were not explicitly
749 represented in this study due to data constraints. Frozen soil is widespread across the

750 region and can exert strong controls on hydrological processes by restricting moisture
751 exchange between deeper soil layers and the atmosphere, reducing soil permeability,
752 and modifying near-surface flow pathways (Li et al., 2025). These effects may influence
753 the partitioning between surface runoff and subsurface flow, particularly in high-
754 elevation permafrost regions with sparse vegetation (Hu et al., 2025). In this study, the
755 elevation-dependent runoff generation patterns identified may partly reflect the
756 integrated influence of frozen soil conditions in these regions. Future studies that
757 explicitly incorporate frozen soil dynamics would help to further disentangle the
758 interacting roles of topography, vegetation, and frozen ground in shaping hydrological
759 responses in alpine basins.

760

761 Second, regarding the assumption of complete mixing in snowmelt runoff tracking, the
762 applied conceptual model represents storages as lumped and homogeneous reservoirs,
763 within which incoming rainfall and snowmelt are assumed to mix instantaneously with
764 pre-event water. Despite its limited ability to explicitly represent rapid snowmelt runoff
765 responses and flow-path heterogeneity at the event scale (Weiler et al., 2018), this
766 assumption is still widely applied in catchment-scale estimates of snowmelt runoff
767 contributions and is regarded as robust at long time scales (Li et al., 2017; Liu et al.,
768 2023; Wu et al., 2021). Importantly, the snowmelt tracker is designed to estimate the
769 long-term average of the fraction of total streamflow that originates from snowmelt,
770 rather than event-scale responses.

771

772 Finally, the use of two study basins entails both advantages and limitations. Focusing
773 on a limited number of basins allows for detailed process interpretation and reduces
774 confounding effects associated with excessive climatic or physiographic diversity, but
775 it also constrains the generalization of the findings (Hrachowitz et al., 2013). The
776 identified runoff generation mechanisms and model performance characteristics should
777 therefore be interpreted as representative of cold, semi-arid alpine basins with similar
778 hydroclimatic and geomorphic settings, rather than as universally applicable.

779 Expanding the analysis to a larger set of basins would be necessary to assess model
780 robustness and transferability more rigorously.

781

782 **7. Conclusions**

783 Hydrological modelling in cold and high-latitude regions remains challenges due to
784 complex cryospheric processes and limited observational data. To address these issues,
785 this study developed and tested a stepwise modelling framework that progressively
786 incorporates key hydrological processes and landscape characteristics, with the aim of
787 improving both predictive performance and process interpretability.

788

789 The results demonstrate that model structure matters. The lumped models (FLEX^L and
790 FLEX^L-S) are insufficient for capturing runoff dynamics in basins with complex
791 topography and heterogeneous vegetation. Although FLEX^D improves simulation by
792 using spatially distributed inputs, it still lacks full physical interpretability. In contrast,
793 the landscape-based FLEX^T model integrates snowpack, topography, and vegetation
794 characteristics, providing more physical meaningful parameterization and a more
795 mechanistic representation of hydrological processes. Validation using SWE further
796 confirms the FLEX^T's ability to capture seasonal dynamics, interannual variability, and
797 key hydrological mechanisms in cryospheric environments. These findings underscore
798 the potential advantages of FLEX^T, particularly in basins with greater ecological or
799 topographic complexity.

800

801 Results from the FLEX^T model indicate that snowmelt runoff accounts for 23.6%±0.7%
802 and 15.9%±1.3% of streamflow in the Bogd Uliastai and Zavkhan Guulin river basins,
803 respectively. Snowmelt runoff dominates streamflow during spring and increases with
804 elevation, underscoring the critical role of topography in shaping runoff generation. In
805 high elevation areas, the lagged snowmelt response leads to a sustained and gradual
806 release of runoff, whereas low elevation areas dominated by rainfall generate rapid
807 runoff. Controlled by distinct dominant hydrological mechanisms, different landscape

808 units contribute unequally to streamflow.

809

810 These findings offer valuable insights into hydrological response mechanisms in cold
811 alpine basins on the Mongolian Plateau. The stepwise modelling framework enhances
812 model realism in cryospheric environments and provides practical support for water
813 resource management, ecological conservation, and climate adaptation in high-latitude
814 and data-scarce regions.

815

816 **Code availability**

817 The code is available upon request to the contact author.

818

819 **Data availability**

820 All data presented in this manuscript are publicly available for download from:
821 Hydrometeorological data (precipitation, runoff, temperature) from the Information and
822 Research Institute of Meteorology, Hydrology, and Environment, available at
823 <http://irimhe.namem.gov.mn>. Arctic Snow Water Equivalent Grid Dataset from the
824 National Tibetan Plateau/Third Pole Environment Data Center, available at
825 <https://estr.cn/18406.11.Snow.tpd.271556>. Shuttle Radar Topography Mission Digital
826 Elevation Model (SRTM-DEM), available at <http://srtm.csi.cgiar.org>. Sentinel-2 10-
827 meter Land Use/Land Cover data from the ESRI Living Atlas, available at
828 <https://livingatlas.arcgis.com/landcover/>. NDVI data were obtained from the United
829 States Geological Survey (USGS) EarthExplorer platform. available at
830 <https://earthexplorer.usgs.gov/>.

831

832 **Author contributions**

833 LY and HG designed the study. BD provided the valuable fieldwork data. LY, YW, HG,
834 and ZD conducted the analyses. LY wrote the paper. All authors discussed the results
835 and the first draft and contributed to the final paper.

836

837 **Acknowledgments**

838 This research is funded by National Key Research and Development Program of China.
839 (2024YFE0113200), the National Natural Science Foundation of China (grant no.
840 42471040). Zheng Duan would like to acknowledge the support from the Crafoord
841 Foundation, Sweden (Grant No.20210552 and No.20240857). This work was
842 performed as part of the IAHS HELPING Working Group on "Development &
843 application of river basin simulators".

844

845 **References**

- 846 Antonelli, A. et al., 2018. Geological and climatic influences on mountain biodiversity. *Nature*
847 *Geoscience*, 11(10): 718-725. DOI:10.1038/s41561-018-0236-z
- 848 Baasanmunkh, S. et al., 2019. Contribution to the knowledge on the flora of northern Mongolia. *Journal*
849 *of Asia-Pacific Biodiversity*, 12(4): 643-660. DOI:https://doi.org/10.1016/j.japb.2019.08.009
- 850 Barnett, T.P., Adam, J.C., Lettenmaier, D.P., 2005. Potential impacts of a warming climate on water
851 availability in snow-dominated regions. *Nature*, 438(7066): 303-309.
852 DOI:10.1038/nature04141
- 853 Beven, K.J., 2012. Rainfall-runoff modeling :the primer. *Rainfall-runoff modelling: the primer*, 15(1):
854 84-96.
- 855 Bormann, H., Breuer, L., Giertz, S., Huisman, J.A., Viney, N.R., 2009. Spatially explicit versus lumped
856 models in catchment hydrology – experiences from two case studies. In: Baveye, P.C., Laba,
857 M., Mysiak, J. (Eds.), *Uncertainties in Environmental Modelling and Consequences for Policy*
858 *Making*. Springer Netherlands, Dordrecht, pp. 3-26.
- 859 Broxton, P.D., van Leeuwen, W.J.D., Biederman, J.A., 2020. Forest cover and topography regulate the
860 thin, ephemeral snowpacks of the semiarid Southwest United States. *Ecohydrology*, 13(4):
861 e2202. DOI:https://doi.org/10.1002/eco.2202
- 862 Chen, J. et al., 2023. Differences in soil water storage, consumption, and use efficiency of typical
863 vegetation types and their responses to precipitation in the Loess Plateau, China. *Science of The*
864 *Total Environment*, 869: 161710. DOI:https://doi.org/10.1016/j.scitotenv.2023.161710
- 865 Cheng, X., Bai, Y., Zhu, J., Han, H., 2020. Effects of forest thinning on interception and surface runoff
866 in *Larix principis-rupprechtii* plantation during the growing season. *Journal of Arid*
867 *Environments*, 181: 104222. DOI:https://doi.org/10.1016/j.jaridenv.2020.104222
- 868 Dharmadasa, V., Kinnard, C., Baraër, M., 2023. Topographic and vegetation controls of the spatial
869 distribution of snow depth in agro-forested environments by UAV lidar. *The Cryosphere*, 17(3):
870 1225-1246. DOI:10.5194/tc-17-1225-2023
- 871 Donovan, M., Monaghan, R., 2021. Impacts of grazing on ground cover, soil physical properties and soil
872 loss via surface erosion: A novel geospatial modelling approach. *Journal of Environmental*
873 *Management*, 287: 112206. DOI:https://doi.org/10.1016/j.jenvman.2021.112206
- 874 Dorjsuren, B. et al., 2024. Trend analysis of hydro-climatic variables in the Great Lakes Depression
875 region of Mongolia. *Journal of Water and Climate Change*, 15(3): 940-957.

876 DOI:10.2166/wcc.2024.379

877 Dorjsuren, B. et al., 2023. Hydro-Climatic and Vegetation Dynamics Spatial-Temporal Changes in the
878 Great Lakes Depression Region of Mongolia, *Water*. DOI:10.3390/w15213748

879 Duethmann, D., Peters, J., Blume, T., Vorogushyn, S., Güntner, A., 2014. The value of satellite-derived
880 snow cover images for calibrating a hydrological model in snow-dominated catchments in
881 Central Asia. *Water Resources Research*, 50(3): 2002-2021.
882 DOI:<https://doi.org/10.1002/2013WR014382>

883 Dwarakish, G.S., Ganasri, B.P., 2015. Impact of land use change on hydrological systems: A review of
884 current modeling approaches. *Cogent Geoscience*, 1(1): 1115691.
885 DOI:10.1080/23312041.2015.1115691

886 Feng, J., Alifujiang, Y., Kozhokulov, S., Jiang, Y., Yang, P., 2025. Quantifying hydrological sensitivity in
887 Central Asia: A multi-factor budyko framework analysis (2000–2020). *Journal of Hydrology:
888 Regional Studies*, 61: 102746. DOI:<https://doi.org/10.1016/j.ejrh.2025.102746>

889 Fenicia, F., Kavetski, D., Savenije, H.H.G., Pfister, L., 2016. From spatially variable streamflow to
890 distributed hydrological models: Analysis of key modeling decisions. *Water Resources
891 Research*, 52(2): 954-989. DOI:<https://doi.org/10.1002/2015WR017398>

892 Fenicia, F., McDonnell, J.J., Savenije, H.H.G., 2008a. Learning from model improvement: On the
893 contribution of complementary data to process understanding. *Water Resources Research*, 44(6).
894 DOI:<https://doi.org/10.1029/2007WR006386>

895 Fenicia, F., Savenije, H.H.G., Matgen, P., Pfister, L., 2008b. Understanding catchment behavior through
896 stepwise model concept improvement. *Water Resources Research*, 44(1).
897 DOI:<https://doi.org/10.1029/2006WR005563>

898 Gao, H., Ding, Y., Zhao, Q., Hrachowitz, M., Savenije, H.H.G., 2017. The importance of aspect for
899 modelling the hydrological response in a glacier catchment in Central Asia. *Hydrological
900 Processes*, 31(16): 2842-2859. DOI:<https://doi.org/10.1002/hyp.11224>

901 Gao, H. et al., 2020. Stepwise modeling and the importance of internal variables validation to test model
902 realism in a data scarce glacier basin. *Journal of Hydrology*, 591: 125457.
903 DOI:<https://doi.org/10.1016/j.jhydrol.2020.125457>

904 Gao, H., Hrachowitz, M., Fenicia, F., Gharari, S., Savenije, H.H.G., 2014. Testing the realism of a
905 topography-driven model (FLEX-Topo) in the nested catchments of the Upper Heihe, China.
906 *Hydrol. Earth Syst. Sci.*, 18(5): 1895-1915. DOI:10.5194/hess-18-1895-2014

907 Gillan, B.J., Harper, J.T., Moore, J.N., 2010. Timing of present and future snowmelt from high elevations
908 in northwest Montana. *Water Resources Research*, 46(1).
909 DOI:<https://doi.org/10.1029/2009WR007861>

910 Gomes, M.N. et al., 2023. HydroPol2D — Distributed hydrodynamic and water quality model:
911 Challenges and opportunities in poorly-gauged catchments. *Journal of Hydrology*, 625: 129982.
912 DOI:<https://doi.org/10.1016/j.jhydrol.2023.129982>

913 Gu, H. et al., 2023. Seasonal catchment memory of high mountain rivers in the Tibetan Plateau. *Nature
914 Communications*, 14(1): 3173. DOI:10.1038/s41467-023-38966-9

915 Gupta, H.V., Kling, H., Yilmaz, K.K., Martinez, G.F., 2009. Decomposition of the mean squared error
916 and NSE performance criteria: Implications for improving hydrological modelling. *Journal of
917 Hydrology*, 377(1): 80-91. DOI:<https://doi.org/10.1016/j.jhydrol.2009.08.003>

918 Hajika, T., Yamakawa, Y., Uchida, T., 2024. Spatial distribution of rainfall–runoff characteristics and
919 peak lag time in high-relief meso-scale mountain catchments where observations are scarce.

920 Hydrological Processes, 38(6): e15177. DOI:<https://doi.org/10.1002/hyp.15177>

921 Hammond, J.C., Harpold, A.A., Weiss, S., Kampf, S.K., 2019. Partitioning snowmelt and rainfall in the
922 critical zone: effects of climate type and soil properties. *Hydrol. Earth Syst. Sci.*, 23(9): 3553-
923 3570. DOI:10.5194/hess-23-3553-2019

924 Hrachowitz, M. et al., 2013. A decade of Predictions in Ungauged Basins (PUB)—a review. *Hydrological
925 Sciences Journal*, 58(6): 1198-1255. DOI:10.1080/02626667.2013.803183

926 Hsu, J. et al., 2025. Impact of land use changes and global warming on extreme precipitation patterns in
927 the Maritime Continent. *npj Climate and Atmospheric Science*, 8(1): 5. DOI:10.1038/s41612-
928 024-00883-z

929 Hu, S. et al., 2025. Groundwater leakage of an endorheic basin with extensive permafrost coverage in
930 the western Mongolian Plateau. *Journal of Hydrology*, 657: 133175.
931 DOI:<https://doi.org/10.1016/j.jhydrol.2025.133175>

932 Immerzeel, W.W., van Beek, L.P.H., Bierkens, M.F.P., 2010. Climate Change Will Affect the Asian Water
933 Towers. *Science*, 328(5984): 1382-1385. DOI:[doi:10.1126/science.1183188](https://doi.org/10.1126/science.1183188)

934 Jenicek, M., Ledvinka, O., 2020. Importance of snowmelt contribution to seasonal runoff and summer
935 low flows in Czechia. *Hydrol. Earth Syst. Sci.*, 24(7): 3475-3491. DOI:10.5194/hess-24-3475-
936 2020

937 Jiao, Y. et al., 2017. Impact of vegetation dynamics on hydrological processes in a semi-arid basin by
938 using a land surface-hydrology coupled model. *Journal of Hydrology*, 551: 116-131.
939 DOI:<https://doi.org/10.1016/j.jhydrol.2017.05.060>

940 Klemeš, V., 1983. Conceptualization and scale in hydrology. *Journal of Hydrology*, 65(1): 1-23.
941 DOI:[https://doi.org/10.1016/0022-1694\(83\)90208-1](https://doi.org/10.1016/0022-1694(83)90208-1)

942 Klemeš, V., 1989. The modelling of mountain hydrology : the ultimate challenge. IAHS-AISH
943 publication, 190: 29-43.

944 Klimek, K., Starkel, L., 1980. Vertical zonality in the Southern Khangai Mountains (Mongolia): result of
945 the polish-mongolian physico-geographical expedition, Vol.I, Geographical studies. Polish
946 Academy of Sciences, Wroclaw.

947 Leibowitz, S.G. et al., 2023. National hydrologic connectivity classification links wetlands with stream
948 water quality. *Nature Water*, 1(4): 370-380. DOI:10.1038/s44221-023-00057-w

949 Li, D., Lettenmaier, D.P., Margulis, S.A., Andreadis, K., 2019. The Role of Rain-on-Snow in Flooding
950 Over the Conterminous United States. *Water Resources Research*, 55(11): 8492-8513.
951 DOI:<https://doi.org/10.1029/2019WR024950>

952 Li, D., Wrzesien, M.L., Durand, M., Adam, J., Lettenmaier, D.P., 2017. How much runoff originates as
953 snow in the western United States, and how will that change in the future? *Geophysical
954 Research Letters*, 44(12): 6163-6172. DOI:<https://doi.org/10.1002/2017GL073551>

955 Li, F., Wang, J., Li, P., Dashtseren, A., 2025. Review of Permafrost Degradation in the Mongolian Plateau.
956 *Land*, 14(2): 383.

957 Liu, J., Zhang, Z., Zhang, M., 2018. Impacts of forest structure on precipitation interception and run-off
958 generation in a semiarid region in northern China. *Hydrological Processes*, 32(15): 2362-2376.
959 DOI:<https://doi.org/10.1002/hyp.13156>

960 Liu, Z., Cuo, L., Sun, N., 2023. Tracking snowmelt during hydrological surface processes using a
961 distributed hydrological model in a mesoscale basin on the Tibetan Plateau. *Journal of
962 Hydrology*, 616: 128796. DOI:<https://doi.org/10.1016/j.jhydrol.2022.128796>

963 Lundquist, J.D., Minder, J.R., Neiman, P.J., Sukovich, E., 2010. Relationships between Barrier Jet

964 Heights, Orographic Precipitation Gradients, and Streamflow in the Northern Sierra Nevada.
965 Journal of Hydrometeorology, 11(5): 1141-1156. DOI:<https://doi.org/10.1175/2010JHM1264.1>

966 Luo, Z. et al., 2022. Widespread root-zone water bypass for various climates and species: Implications
967 for the ecohydrological separation understanding. Agricultural and Forest Meteorology, 324:
968 109107. DOI:<https://doi.org/10.1016/j.agrformet.2022.109107>

969 Ni, J. et al., 2025. Duration of vegetation green-up response to snowmelt on the Tibetan Plateau.
970 Biogeosciences, 22(11): 2637-2651. DOI:10.5194/bg-22-2637-2025

971 Oki, T., Kanae, S., 2006. Global Hydrological Cycles and World Water Resources. Science, 313(5790):
972 1068-1072. DOI:[doi:10.1126/science.1128845](https://doi.org/10.1126/science.1128845)

973 Qin, J., Yang, B., Ding, Y., Cui, J., Zhang, Y., 2025. Assessment of runoff generation capacity and total
974 runoff contribution for different landscapes in alpine and permafrost watershed. CATENA, 249:
975 108643. DOI:<https://doi.org/10.1016/j.catena.2024.108643>

976 Ragettli, S., Cortés, G., McPhee, J., Pellicciotti, F., 2014. An evaluation of approaches for modelling
977 hydrological processes in high-elevation, glacierized Andean watersheds. HYDROLOGICAL
978 PROCESSES, 28(23): 5674-5695. DOI:10.1002/hyp.10055

979 Roebroek, C.T.J., Melsen, L.A., Hoek van Dijke, A.J., Fan, Y., Teuling, A.J., 2020. Global distribution
980 of hydrologic controls on forest growth. Hydrol. Earth Syst. Sci., 24(9): 4625-4639.
981 DOI:10.5194/hess-24-4625-2020

982 Savenije, H.H.G., 2010. HESS Opinions "Topography driven conceptual modelling (FLEX-Topo)".
983 Hydrol. Earth Syst. Sci., 14(12): 2681-2692. DOI:10.5194/hess-14-2681-2010

984 Seibert, J., McDonnell, J.J., 2002. On the dialog between experimentalist and modeler in catchment
985 hydrology: Use of soft data for multicriteria model calibration. Water Resources Research,
986 38(11): 23-1-23-14. DOI:<https://doi.org/10.1029/2001WR000978>

987 Sivapalan, M., 2009. The secret to 'doing better hydrological science': change the question!
988 Hydrological Processes, 23(9): 1391-1396. DOI:<https://doi.org/10.1002/hyp.7242>

989 Sivapalan, M., Zhang, L., Vertessy, R., Blöschl, G., 2003. Downward approach to hydrological prediction.
990 Hydrological Processes, 17(11): 2099-2099. DOI:<https://doi.org/10.1002/hyp.1426>

991 Stahl, K., Moore, R.D., Floyer, J.A., Asplin, M.G., McKendry, I.G., 2006. Comparison of approaches for
992 spatial interpolation of daily air temperature in a large region with complex topography and
993 highly variable station density. Agricultural and Forest Meteorology, 139(3): 224-236.
994 DOI:<https://doi.org/10.1016/j.agrformet.2006.07.004>

995 Stephens, C.M., Lall, U., Johnson, F.M., Marshall, L.A., 2021. Landscape changes and their hydrologic
996 effects: Interactions and feedbacks across scales. Earth-Science Reviews, 212: 103466.
997 DOI:<https://doi.org/10.1016/j.earscirev.2020.103466>

998 Stocker, B.D. et al., 2023. Global patterns of water storage in the rooting zones of vegetation. Nature
999 Geoscience, 16(3): 250-256. DOI:10.1038/s41561-023-01125-2

1000 Sun, N. et al., 2022. Forest Canopy Density Effects on Snowpack Across the Climate Gradients of the
1001 Western United States Mountain Ranges. WATER RESOURCES RESEARCH, 58(1).
1002 DOI:10.1029/2020WR029194

1003 Tarasova, L., Knoche, M., Dietrich, J., Merz, R., 2016. Effects of input discretization, model complexity,
1004 and calibration strategy on model performance in a data-scarce glacierized catchment in Central
1005 Asia. Water Resources Research, 52(6): 4674-4699.
1006 DOI:<https://doi.org/10.1002/2015WR018551>

1007 Volpe, V., Marani, M., Albertson, J.D., Katul, G., 2013. Root controls on water redistribution and carbon

1008 uptake in the soil–plant system under current and future climate. *Advances in Water Resources*,
1009 60: 110-120. DOI:<https://doi.org/10.1016/j.advwatres.2013.07.008>

1010 Vrugt, J.A., Gupta, H.V., Bouten, W., Sorooshian, S., 2003. A Shuffled Complex Evolution Metropolis
1011 algorithm for optimization and uncertainty assessment of hydrologic model parameters. *Water*
1012 *Resources Research*, 39(8). DOI:<https://doi.org/10.1029/2002WR001642>

1013 Weiler, M., Seibert, J., Stahl, K., 2018. Magic components—why quantifying rain, snowmelt, and icemelt
1014 in river discharge is not easy. *Hydrological Processes*, 32(1): 160-166.
1015 DOI:<https://doi.org/10.1002/hyp.11361>

1016 Wicki, A., Lehmann, P., Hauck, C., Stähli, M., 2023. Impact of topography on in situ soil wetness
1017 measurements for regional landslide early warning – a case study from the Swiss Alpine
1018 Foreland. *Nat. Hazards Earth Syst. Sci.*, 23(3): 1059-1077. DOI:10.5194/nhess-23-1059-2023

1019 Wu, X. et al., 2021. Analysis of seasonal snowmelt contribution using a distributed energy balance model
1020 for a river basin in the Altai Mountains of northwestern China. *Hydrological Processes*, 35(3):
1021 e14046. DOI:<https://doi.org/10.1002/hyp.14046>

1022 Xiong, C. et al., 2023. Improved global 250 m 8-day NDVI and EVI products from 2000–2021 using the
1023 LSTM model. *Scientific Data*, 10(1): 800. DOI:10.1038/s41597-023-02695-x

1024 Xue, D., Tian, J., Zhang, B., Kang, W., He, C., 2025. Evaluating the effect of vegetation type and
1025 topography on infiltration process in an arid mountainous area: Insights from continuous soil
1026 moisture monitoring network. *Agricultural Water Management*, 315: 109537.
1027 DOI:<https://doi.org/10.1016/j.agwat.2025.109537>

1028 Ye, S. et al., 2023. From rainfall to runoff: The role of soil moisture in a mountainous catchment. *Journal*
1029 *of Hydrology*, 625: 130060. DOI:<https://doi.org/10.1016/j.jhydrol.2023.130060>

1030 Zeng, X., Peng, X., Liu, T., Dai, Q., Chen, X., 2024. Runoff generation and erosion processes at the rock–
1031 soil interface of outcrops with a concave surface in a rocky desertification area. *CATENA*, 239:
1032 107920. DOI:<https://doi.org/10.1016/j.catena.2024.107920>

1033 Zhang, W., Kang, S.-c., Shen, Y.-p., He, J.-q., Chen, A.-a., 2017. Response of snow hydrological
1034 processes to a changing climate during 1961 to 2016 in the headwater of Irtysh River Basin,
1035 Chinese Altai Mountains. *Journal of Mountain Science*, 14(11): 2295-2310.
1036 DOI:10.1007/s11629-017-4556-z

1037 Zhao, R., 1992. The Xinanjiang model applied in China. *Journal of Hydrology*, 135(1): 371-381.
1038 DOI:[https://doi.org/10.1016/0022-1694\(92\)90096-E](https://doi.org/10.1016/0022-1694(92)90096-E)

1039 Zhong, X.-Y. et al., 2021. Impacts of landscape and climatic factors on snow cover in the Altai Mountains,
1040 China. *Advances in Climate Change Research*, 12(1): 95-107.
1041 DOI:<https://doi.org/10.1016/j.accre.2021.01.005>

1042 Zhou, S., Yu, B., Lintner, B.R., Findell, K.L., Zhang, Y., 2023. Projected increase in global runoff
1043 dominated by land surface changes. *Nature Climate Change*, 13(5): 442-449.
1044 DOI:10.1038/s41558-023-01659-8

1045